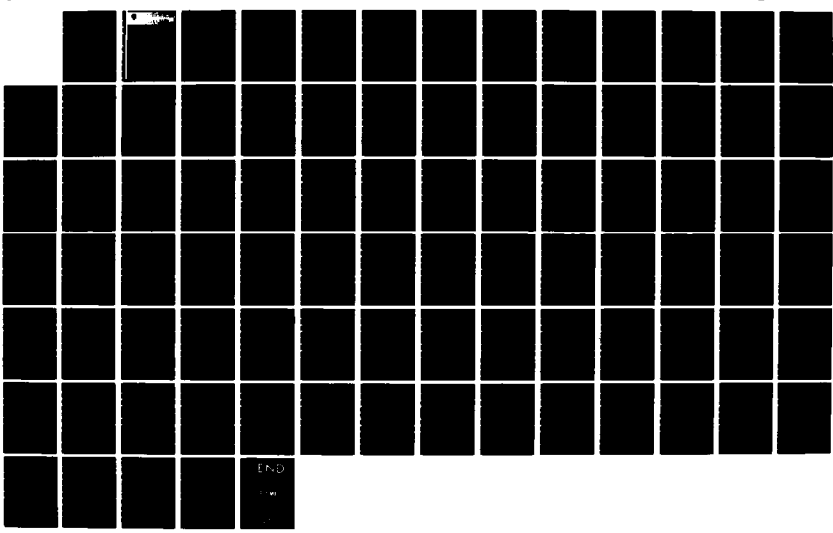
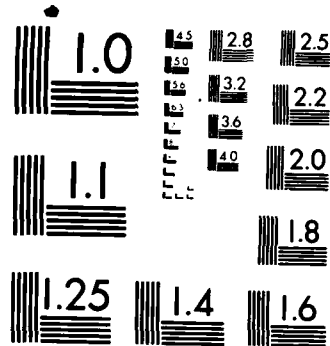
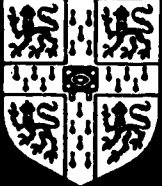


AD-A161 947 DEFORMATION AND FRACTURE MAPS FOR CELLULAR MATERIALS 1/1
AND SOLID POLYMERS(U) CAMBRIDGE UNIV (ENGLAND) DEPT OF
ENGINEERING M F ASHBY ET AL 31 OCT 85
UNCLASSIFIED CUED/C/MAPS/TR118 DAJA45-84-M-8426 F/G 11/9 NL





MICROCOPY RESOLUTION TEST CHART
NATIONAL BUREAU OF STANDARDS-1963-A



CAMBRIDGE UNIVERSITY

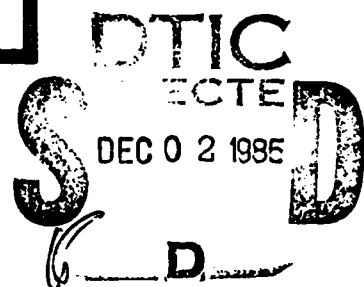
AD-A161 947

DEFORMATION MECHANISM MAPS FOR
CELLULAR MATERIALS
AND SOLID POLYMERS

M.F. Ashby, P.W.R. Beaumont, L.J. Gibson,
D.G. Gilbert and S.K. Maiti

CUED/C/MATS/TR118 (October 1985)

Cambridge University Engineering Department
Trumpington Street, Cambridge CB2 1PZ, U.K.



Engineering Department

DTIC FILE COPY

DISTRIBUTION STATEMENT A

Approved for public release
Distribution Unlimited

85 11 23 031

(C)

DEFORMATION MECHANISM MAPS FOR
CELLULAR MATERIALS
AND SOLID POLYMERS

M.F. Ashby, P.W.R. Beaumont, L.J. Gibson,
D.G. Gilbert and S.K. Maiti

CUED/C/MATS/TR118 (October 1985)

Cambridge University Engineering Department
Trumpington Street, Cambridge CB2 1PE, U.K.

This document has been approved
for public release and sale; its
distribution is unlimited.

Unclassified

SECURITY CLASSIFICATION OF THIS PAGE (When Data Entered)

REPORT DOCUMENTATION PAGE		READ INSTRUCTIONS BEFORE COMPLETING FORM
1. REPORT NUMBER	2. GOVT ACCESSION NO.	3. RECIPIENT'S CATALOG NUMBER
		AD-A161 947
4. TITLE (and Subtitle) Deformation and Fracture Maps for Cellular Materials and Solid Polymers		5. TYPE OF REPORT & PERIOD COVERED Final Technical 18 Sep 84-10 Sep 85
7. AUTHOR(s) Professor Michael F. Ashby Dr. Peter Beaumont		6. PERFORMING ORG. REPORT NUMBER
9. PERFORMING ORGANIZATION NAME AND ADDRESS U.S. Army Research Development & Standardization Group-UK Box 65 FPO NY 09510-1500		10. PROGRAM ELEMENT, PROJECT, TASK AREA & WORK UNIT NUMBERS 61102A 1L161102BII57-04
11. CONTROLLING OFFICE NAME AND ADDRESS U.S. Army Research Office P.O. Box 12211 Research Triangle Park, NC 27709		12. REPORT DATE 31 October, 1985
14. MONITORING AGENCY NAME & ADDRESS(if different from Controlling Office) Approved for public release; distribution unlimited		13. NUMBER OF PAGES
		15. SECURITY CLASS. (of this report) unclassified
		15a. DECLASSIFICATION/DOWNGRADING SCHEDULE
16. DISTRIBUTION STATEMENT (of this Report) <div style="border: 1px solid black; padding: 5px; width: fit-content;">This document has been approved for public release and sale; its distribution is unlimited.</div>		
17. DISTRIBUTION STATEMENT (of the abstract entered in Block 20, if different from Report)		
18. SUPPLEMENTARY NOTES <i>cont'd</i>		
19. KEY WORDS (Continue on reverse side if necessary and identify by block number) DEFORMATION, FRACTURE, MAPS, CELLULAR MATERIALS, POLYMERS, ENERGY-ABSORPTION.		
20. ABSTRACT (Continue on reverse side if necessary and identify by block number) Experimental data and deformation models are combined to develop mechanism-mode maps for cellular materials. They are used to construct energy-absorption diagrams for use in design and selection of materials. Alternative mechanisms and constitutive equations are used to develop deformation-mechanism maps for solid polymers. The map summarises the small-strain mechanical behaviour over a wide range of time and temperature.		

DEFORMATION AND ENERGY ABSORPTION DIAGRAMS FOR CELLULAR SOLIDS

S.K. Maiti*†, L.J. Gibson+ and M.F. Ashby*

*Cambridge University,
Engineering Department,
Trumpington Street,
Cambridge CB2 1PZ
England

+Dept. of Civil Engineering,
University of British Columbia,
Vancouver B.C., Canada

†On leave from
I.I.T., Bombay, India.

ABSTRACT

The mechanical properties of 3 types of cellular solids (flexible, plastic and brittle) have been measured as a function of density. The results are compared with models for the stiffness, strength and densification; and constitutive laws are developed. Data and models for each type of cellular solid are combined to develop mechanism-mode maps which summarize the properties in a single diagram. Natural cellular materials fit the same pattern; maps are presented, as an example, for wood. The maps help in design and in the selection of materials for load-bearing and energy-absorbing applications.

Original Drafted by E. K.

Accession For	
NTIS CRA&I	<input checked="" type="checkbox"/>
CAC TAB	<input type="checkbox"/>
Unannounced	<input type="checkbox"/>
Classification	
By	
Distribution	
Availability Codes	
Avail and/or Dist	Special



TABLE 1: SYMBOLS AND UNITS

σ	Applied compressive stress	(N/m ²)
ϵ	Nominal compressive strain	(-)
ρ	Initial density of cellular solid	(kg/m ³)
$\rho (\epsilon)$	Density after compressive strain ϵ	(kg/m ³)
ρ_s	Density of cell wall material	(kg/m ³)
ρ/ρ_s	Relative density	(-)
E^*	Young's modulus of cellular solid	(N/m ²)
E_s^*	Young's modulus of cell-wall material	(N/m ²)
σ_{el}^*	Elastic collapse or plateau stress of elastomeric foam	(N/m ²)
σ_{pl}^*	Plastic collapse or plateau stress of plastic foam	(N/m ²)
σ_y^*	Yield strength of cell-wall material	(N/m ²)
σ_f^*	Crushing stress of brittle foam	(N/m ²)
σ_f	Modulus of rupture of cell-wall material	(N/m ²)
t	Cell wall thickness	(m)
l	Cell size or cell wall length	(m)
$l(\epsilon)$	Length of uncollapsed members at strain ϵ	(m)
l_0	Initial length of an uncollapsed member	(m)
I	Second moment of area of cell wall or edge	(m ⁴)
F	Force acting on a cell wall	(N)
F_{cr}	Euler buckling load for cell wall	(N)
M_p	Fully plastic moment of cell wall	(Nm)
M_f	Moment which will just fracture cell wall	(Nm)
$C_1 - C_8$	Dimensionless constants	(-)
h_0	Initial height of sample	(m)
h	Height after strain ϵ	(m)
P	Load	(N)

1. INTRODUCTION

Polymeric foams have certain characteristic mechanical properties. *Elastomeric or flexible foams*, in simple compression, are linear-elastic to a strain of about 5 %. Then the cell walls buckle and the foam collapses at a nearly constant stress (giving a non-linear elastic deformation) until the cell walls touch and the stress-strain curve rises steeply. *Rigid polymers and metals*, when foamed, have a similar stress-strain curve, but for a different reason. Like flexible foams, they are linear-elastic to a strain of roughly 5 %. Then they suffer plastic collapse, compressing plastically at a nearly constant stress until the cell walls touch, and the stress-strain curve rises steeply. *Brittle foams*, too, show an initial linear-elastic regime. But when the stress is reached at which cell walls fracture, the stress-strain curve becomes irregular (though roughly horizontal) and the foam crushes at (roughly) constant load.

Fig. 1 shows, schematically, the structure of cellular solids. Some have *open cells*: the solid material is distributed as little beams which form the cell edges. Others have *closed cells*: the solid is distributed as little plates which form the cell faces. The mechanical properties reflect, to some extent, this distribution. In practice, most man-made foams (even those with closed cell faces) behave as if they had open cells because surface tension draws much of the solid material into the cell-edges during manufacture. For this reason, we discuss open-cell foams in detail, but treat closed cell foams only in passing.

The mechanical properties of a cellular solid can be related to the mechanics of bending, buckling, plastic collapse and brittle fracture of its cell walls. Each part of the stress-strain curve can be modelled (1,2,3,4). The models give equations for Young's modulus E^* ,

the elastic buckling stress σ_{el}^* , the plastic collapse stress σ_{pl}^* , the crushing strength σ_f^* , and terminal rise in strength, in terms of the density and properties of the material of which the foam is made.

This paper seeks to test and extend these models, (checking them against data from the literature and new data, described below), to derive constitutive laws for design with cellular solids, and to develop diagrams which summarise the overall mechanical response of each type. Symbols are defined in Table 1.

2. EXPERIMENTAL RESULTS

2.1 Foamed Plastics and Ceramics

We tested samples of commercial flexible foams (a polyethylene and a polyurethane), samples of a commercial rigid foam (a polymethylacrylimid) and an experimental batch of a brittle ceramic foam (mullite). The materials, their origins and the properties of the cell walls are listed in Table 2. Their structures are shown in Fig. 2.

Compression tests were carried out on blocks of foam of a convenient size (the size depending on the stiffness), at a temperature of 18°C and a strain-rate of roughly $2 \times 10^{-3}/\text{s}$. Results are shown in Figs. 3 to 6. The axes are the nominal stress (the load P divided by the initial section A_0):

$$\sigma = \frac{P}{A_0} \quad (1)$$

and the nominal compressive strain:

$$\epsilon = \frac{h_0 - h}{h_0} \quad (2)$$

where h is the height of the sample after a strain ϵ , and h_0 is the original height. When foams are compressed beyond a strain of a few %, there is almost no lateral spreading, so the nominal and true stresses are, for all practical purposes, identical. The nominal compressive strain is, of course, limited to the range 0 to 1.

All the stress-strain curves show three regions: a *linear elastic region*; a long *plateau* where the stress is almost independent of strain; and (for all but the brittle foams) a final region of *densification* in which the stress-strain curve rises steeply. Young's modulus E^* of the rigid foams was measured by using clip gauges. The density ρ of each foam was measured by conventional methods. Mean values of ρ , E^* and of the plateau stress σ^* are listed in Table 3.

2.2 Woods

We also tested a number of woods, chosen to give a range of relative densities between 0.05 and 0.5. Samples of well-seasoned woods, roughly 20 mm \times 20 mm \times 40 mm, were cut with the long direction parallel to a radius of the trunk (Fig. 7) and parallel to the axis of the trunk (Fig. 8). The samples were stored for 10 days to reach an equilibrium moisture content (roughly 12 %) and tested in compression at 18 °C and a strain rate close to $10^{-3}/\text{s}$.

3. MODELS FOR THE MECHANICAL PROPERTIES

When a cellular material is compressed, the cell walls deform. The deformation modes (bending, buckling, plastic collapse and fracture) are known from studies of model cells (2). Two-dimensional models (shown in insets of subsequent figures) can be analysed accurately (2). With this knowledge, a kind of dimensional analysis of 3-dimensional cellular solids (1, 3, 4) becomes possible. This analysis,

summarised briefly below, involves, in each case, a single geometric constant which must be determined by experiment. The data are analysed to give this constant.

3.1 Stiffness

When a foam is loaded, the cell walls at first bend (1,2,5,6,7) as shown in the inset of Fig. 9. A force F , applied as shown, causes the non-vertical beams to deflect by an amount, δ , which can be calculated from elastic beam theory:

$$\delta = \frac{C_1 F l^3}{E_s I} \quad (3)$$

Here C_1 is a factor which depends on cell-wall geometry. A similar deflection occurs in a 3-dimensional cellular solid, like those shown in Fig. 1. Considering the open-cell foam, the force F is proportional to σl^2 where σ is the remote stress; and the strain ϵ is proportional to δ/l . The second moment of area, I , of a cell edge with section t^2 is $t^{4/2}$ so that the modulus E^* of the foam is:

$$E^* \propto E_s \frac{t^4}{l^4} \quad (4)$$

The dimensions of the open cells are related to the relative density of the foam ρ/ρ_s , by:

$$\rho/\rho_s \propto t^2/l^2 \quad (5)$$

giving:

$$\frac{E^*}{E_s} = C_2 \left(\frac{\rho}{\rho_s} \right)^2 \quad (6)$$

where C_2 is a constant. The shear modulus scales in a similar way, because shear deformation in a foam also causes simple bending of the cell walls. (For closed cells, $I \propto lt^3$ and $\rho/\rho_s \propto t/l$ giving instead $E^*/E_s \propto (\rho/\rho_s)^3$).

Data are compared with eqn. (6) in Fig. 9. The full line is a plot of eqn. (6) with $C_2 = 1$. It gives a good description of a wide range of materials and densities. (We find that plastic foams deviate systematically towards the line $E^*/E_s = (\rho/\rho_s)^{3/2}$, because, we believe, some limited plasticity occurs even under small loads. Section 3.3, below, explains the power of $^{3/2}$.)

Poissons ratios ν have been measured for cellular solids (1,3). In the linear-elastic regime, $\nu \approx \frac{1}{3}$, although in the plateau regime it is almost zero.

3.2 Elastic Buckling

Flexible foams show extensive non-linear elasticity. It is caused by the *elastic buckling* of the cell walls (8,18), as shown in the inset of Fig. 10, and it is this that gives the plateau of the stress-strain curve for elastomeric foams.

The critical load at which a column of length l , Young's modulus E_s and second moment of area I buckles, is given by Euler's formula:

$$F_{cr} \propto \frac{E_s I}{l^2} \quad (7)$$

If this load is reached for a layer of cells spanning the section, they buckle, initiating the *elastic collapse* of the foam. For the 3-dimensional open-cell foam of Fig. 1 the stress σ_{el}^* at which

this occurs is proportional to F_{cr}/l^2 . Using the facts that $I \propto t^4$ and $\rho/\rho_s \propto (t/l)^2$ we obtain the elastic collapse, or plateau, stress:

$$\frac{\sigma_{el}^*}{E_s} = C_3 \left(\frac{\rho}{\rho_s}\right)^2 \quad (8)$$

It is valid for relative densities below 0.3. At higher densities, the cell walls are too short and stocky to buckle; instead they yield or crush.

Data for σ_{el}^* for elastomeric foams are compared with eqn. (8) in Fig. 10. They are well fitted by the equation with $C_3 = 0.05$.

3.3 Plastic Collapse

If the cell-wall material yields plastically, as do metals and many polymers, then the foam as a whole shows a plateau caused by *plastic collapse*. It occurs when the moment on the inclined cell walls exceeds the fully plastic moment, creating plastic hinges (2,3,19,20) as shown in the inset of Fig. 11. For a beam of square section of side t , the fully plastic moment is:

$$M_p = \frac{1}{4} \sigma_y t^3 \quad (9)$$

The moment is proportional to Fl , and (as before) the force F is proportional to σl^2 . Combining these results with eqn. (5) we find the plastic collapse, or plateau stress σ_{pl}^* to be:

$$\frac{\sigma_{pl}^*}{\sigma_y} = C_4 \left(\frac{\rho}{\rho_s}\right)^{\frac{3}{2}} \quad (10)$$

Data for the plateau-stress of plastic foams are plotted in Fig. 11. They are well fitted by eqn. (10) with $C_4 = 0.3$ for relative densities less than 0.6 (1); at higher densities the cell edges are too short and stocky to bend plastically; instead, they shear.

3.4 Brittle Crushing

Brittle foams (ceramics, and certain rigid polymers) collapse by yet other mechanisms: brittle crushing in compression (23), brittle fracture in tension (24,25). Let the modulus of rupture (the maximum surface stress at the instant of fracture) for the cell-wall material be σ_f . Then a cell wall will fail as shown in the inset to Fig. 12 when the moment acting on it exceeds:

$$M_f = \frac{1}{6} \sigma_f t^3$$

The moment due to F is proportional to $F\ell$, and the stress to F/ℓ^2 . Combining these with eqn. (5) gives the crushing strength σ_f^* of the foam:

$$\frac{\sigma_f^*}{\sigma_f} = C_7 \left(\frac{\rho}{\rho_s}\right)^{\frac{3}{2}} \quad (11)$$

The limited experimental data, shown in Fig. 12, are consistent with $C_7 = 0.65$ but are insufficient to give much confidence in eqn. (11). But observations, reviewed elsewhere (4), suggest that the model has the correct physical basis, and we shall employ it in subsequent sections.

3.5 Densification and the Shape of the Stress-Strain Curve

The plateau ends when the folding cell walls begin to touch. During elastic buckling or plastic collapse, the foam compresses axially with almost no lateral spreading ($v \approx 0$). Then simple geometry gives the relative density $\rho(\epsilon)/\rho_s$ after a nominal compressive strain ϵ as:

$$\frac{\rho(\epsilon)}{\rho_s} = \frac{\rho}{\rho_s} \left(\frac{1}{1 - \epsilon} \right) \quad (12)$$

where ρ/ρ_s is the initial relative density. Densification is complete, and the stress-strain curve becomes almost vertical, when $\rho(\epsilon)/\rho_s = 1$, when the strain is:

$$\epsilon_f = 1 - \rho/\rho_s \quad (13)$$

We find experimentally that the end of the plateau corresponds to $\rho(\epsilon)/\rho_s \approx 0.33$ (the solid occupies $\frac{1}{3}$ of the total volume) when the strain is:

$$\epsilon_s = 1 - 3(\rho/\rho_s) \quad (14)$$

Consider now the shape of the stress-strain curve for flexible foams. In any sample of the foam, there is a distribution of cell edge-lengths and angles. The plateau starts when a layer of cells (those with longest, or most favourably oriented edges) buckle (eqn. 7). A small increase in stress is needed to cause more cell edges (those which are slightly shorter) to buckle. We postulate that the length of the edges which are about to buckle after a strain ϵ , $\ell(\epsilon)$, is given by:

$$\ell(\varepsilon) = \ell_0 \frac{(1 - (\frac{\rho(\varepsilon)}{\rho_s})^{\frac{1}{3}})}{1 - (\rho/\rho_s)^{\frac{1}{3}}} \quad (15)$$

(The value $\ell(\varepsilon)$ ranges from ℓ_0 at the start of deformation to zero when full density is reached.) Using eqn. (12) we obtain:

$$\ell(\varepsilon) = \ell_0 \frac{(1 - (\frac{\rho}{\rho_s} \frac{1}{(1-\varepsilon)})^{\frac{1}{3}})}{1 - (\rho/\rho_s)^{\frac{1}{3}}} \quad (16)$$

The argument of Section 3.2 can now be repeated. The force F on the cell wall is related to ℓ_0 throughout the test by $F = \sigma \ell_0^2$. Collapse of cells with edge length ℓ (given by eqn. (16)) occurs when this force exceeds the buckling load given by eqn. (7). Combining these equations gives:

$$\frac{\sigma}{E_s} = 0.05 \left(\frac{\rho}{\rho_s} \right)^2 \left\{ \frac{1 - (\rho/\rho_s)^{\frac{1}{3}}}{1 - (\rho/\rho_s \frac{1}{(1-\varepsilon)})^{\frac{1}{3}}} \right\}^2 \quad (17)$$

which reduces to our original eqn. (8) at small strains, but becomes infinite (approximating E_s) at the strain given by eqn. (13).

A similar analysis can be made for plastic foams. We postulate that the length of the beams which are about to bend plastically decreases as strain proceeds (because the long ones bend first). If the length at a strain ε is given (as before) by eqn. (16), then by the argument of Section 3.3, the strength of a plastic foam follows:

$$\frac{\sigma}{E_s} = 0.3 \frac{\sigma_y}{E_s} \left(\frac{\rho}{\rho_s} \right)^{\frac{3}{2}} \left\{ \frac{1 - (\rho/\rho_s)^{\frac{1}{3}}}{1 - (\rho/\rho_s) \left(\frac{1}{1 - \epsilon} \right)^{\frac{1}{3}}} \right\} \quad (18)$$

This reduces to eqn. (10) at small strains, but becomes infinite (approximating E_s) as the foam is compressed to the solid density (eqn. 13).

These two results give an approximate description of the stress-strain curves for flexible and for rigid-plastic foams, in the fields of plastic collapse and densification. They are combined with the equations for linear-elasticity, in the next section, to construct deformation-mode maps and energy-absorption diagrams.

4. CONSTRUCTION OF DEFORMATION-MODE MAPS

We have seen that when an elastomeric foam is compressed, it first deforms in a linear-elastic way; then its cells buckle to give non-linear elasticity; and, finally, the cells collapse completely and the stress rises rapidly as their faces and edges are forced together. A plastic foam behaves in a somewhat similar way, except that linear elasticity is now followed by plastic collapse, and the ultimate forcing together of the cell walls. With brittle foams, progressive crushing can again lead to a plateau which ends when the material is completely crushed. We have seen, too, that each of these processes can be modelled adequately by using classical beam theory to analyse the deformation of cell walls. The analysis relates foam properties

to the relative density (ρ/ρ_s) and to the properties of the material of which the foam is made. The relations, summarised in Table 4, suggest a normalisation which brings the properties of foams with the same relative densities into coincidence. Then the properties of an entire family of foams can be shown as a *deformation mode map* (4), of which Figs. 13 to 16 are examples. The map has axes of normalised compressive stress σ/E_s , and the compressive strain ϵ . It shows the fields in which each mode of deformation (linear elasticity, non-linear elasticity, plastic collapse and so forth) is dominant. Superimposed on the fields are stress-strain contours for constant (initial) relative density.

4.1 Elastomeric Foams

Figs. 13 and 14 show mechanism-mode maps for elastomeric foams. Fig. 13 shows the experimental stress-strain curves for polymeric foams; Fig. 14 is based on the theory alone. Mechanism field boundaries (heavy lines) are shown on both figures. They were constructed as follows.

The linear-elastic regime ends when elastic buckling begins. Using eqns. (6) and (8), and the fact that $\sigma = E\epsilon$ in the linear-elastic region, we obtain the strain corresponding to the boundary of the linear-elastic field:

$$\epsilon = C_3 = 0.05$$

At relative densities above about 0.3 the cell walls become so stocky that they can no longer buckle elastically. The field boundary thus bends until it is tangent to the linear-elastic loading line for $\rho/\rho_s = 0.3$.

Once elastic buckling starts, the stress is related to the strain by eqn. (17). We define the transition from buckling to densification

as the line at which the relative density has reached $\frac{1}{3}$. Then, from eqn. (14) and (17) the equation of the transition is:

$$\frac{\sigma}{E_s} = 5.9 \times 10^{-2} (1 - \epsilon)^2 \left\{ 1 - \left(\frac{1 - \epsilon}{3} \right)^{\frac{1}{3}} \right\}^2 \quad (19)$$

It is plotted as a heavy line, sloping down from left to right on the figures.

Fig. 14 shows a theoretical map. The contours are stress-strain curves for foams of relative density between 0.01 and 0.4. They show a linear elastic regime (eqn. 6) and a plateau corresponding to elastic buckling; they start to bend upwards when densification starts (eqn. 17); and they approach a limiting slope of E_s when densification is complete (eqn. 13). Within the field of elastic buckling the material exists in two states at almost the same stress (the linear-elastic state and the densified state); it is like the p-V response of an ideal gas (or the temperature-entropy diagram for steam) in which gas and liquid states can co-exist. The material deforms by the formation of densified bands which thicken, at constant stress, as the strain is increased, until the entire material has reached the dense state.

The figure describes the overall response of all isotropic, flexible foams in compression. In tension, flexible foams are roughly linear-elastic to rupture.

4.2 Rigid Plastic Foams

Plastic foams, like the elastic ones, show three regions: linear elasticity, plastic collapse and densification - though now the strain beyond the linear-elastic regime is not recoverable. Figs. 15 and 16 are a pair of maps, one showing our experimental stress-strain curves for plastic foams, the other, based on the theory alone. Mechanism field-

boundaries are superimposed on the stress-strain curves.

The boundary of the linear-elastic field (heavy line) is obtained from the equation for linear elasticity (eqn. 6) and that for plastic collapse (eqn. 10); its equation is:

$$\frac{\sigma}{E_s} = (0.3 \frac{\sigma_y}{E_s})^4 \frac{1}{\epsilon^3} \quad (20)$$

In constructing the map we have taken σ_y/E_s to be 0.10 (a fairly typical value). Next to the linear-elastic field is the field of plastic collapse. As before, two states of strain co-exist at almost the same stress, so that complete collapse of part of the structure can occur while the rest is still elastic; the bands of dense material broaden with increasing strain. We define the transition from collapse to densification as the line at which the relative density has reached $\frac{1}{3}$. Then, from eqn. (14) and eqn. (18), the equation of the transition line is:

$$\frac{\sigma}{E_s} = 0.19 \frac{\sigma_y}{E_s} (1 - \epsilon)^{\frac{3}{2}} \left\{ 1 - \left(\frac{1 - \epsilon}{3} \right)^{\frac{1}{3}} \right\} \quad (21)$$

It is plotted as a heavy line sloping down from left to right on Figs. 15 and 16.

Fig. 16 shows a theoretical map for plastic foams with $\sigma_y/E_s = 0.10$. It shows fields of elastic deformation, plastic collapse and densification. Superimposed on the fields are stress-strain curves for foams with densities from 0.01 to 0.4.

The figure shows the overall response of isotropic, plastic foams in compression. It is less general than the map for elastomeric foams because it must be constructed for a particular value of σ_y/E_s . But the equations show that the boundaries are not very sensitive to its value, and, for a given material, the diagram shows the behaviour for all densities.

The behaviour of plastic foams in tension resembles that in compression, truncated by fracture.

4.3 Brittle Foams

Rigid foams show linear-elastic behaviour to fracture. In compression, the foam crushes at constant stress (eqn. 11), and since the crushing equation has the same form as that for plastic collapse, the behaviour will resemble that of Figs. 15 and 16. If the foam is contained, it will densify at the strain given approximately by eqn. (18), with σ_y/E_s replaced by σ_f/E_s .

In tension, linear elastic behaviour is truncated by fast, brittle fracture. The fracture mechanics of foams (28) need not concern us here.

4.4 Woods

These ideas can be applied, in an approximate way, to the compressive deformation of wood. Woods are cellular solids, composed of mixed polymers (cellulose, lignin, hemicellulose), and with a relative density ranging from less than 0.05 (balsas) to almost 1 (lignum vitae). Compressed across the grain, wood behaves like a rigid-plastic foam. Stress-strain curves for the woods we tested are shown in Fig. 17, plotted on axes of σ/E_s and ϵ (data in Tables 2 and 3).

The field boundaries of Fig. 17 were constructed as follows. In radial compression, Young's modulus for woods is found to follow the same law as elastic foams (29):

$$E^* = 10 \left(\frac{\rho}{\rho_s}\right)^2 \text{ GN/m}^2 \quad (22)$$

Compressive collapse in the radial direction eqn. (29) starts at the stress:

$$\sigma^* = 135 \left(\frac{\rho}{\rho_s}\right)^2 \text{ MN/m}^2 \quad (23)$$

$$\epsilon = 0.004$$

When woods are compressed axially, they collapse by a process which involves the kinking (30) or fracture (29,30) of the cell walls.

This occurs at essentially *constant* stress until a critical state is reached, when the stress-strain curve bends sharply upwards.

Experimentally, we find that the bend upwards occurs at a strain ϵ_c corresponding to a density of roughly 0.5:

$$\epsilon_c = 1 - 2 \left(\frac{\rho}{\rho_s} \right)$$

Combining this with eqn. (27) gives the field boundary:

$$\frac{\sigma^*}{E_s} = 2 \times 10^{-3} (1 - \epsilon)$$

It is plotted as a heavy line on Fig. 18. The figure summarises the compressive behaviour of woods in the axial direction. Both diagrams allow, by interpolation, or the use of the equations, the approximate prediction of the stress-strain curve for woods of other densities.

S. CONSTRUCTION OF ENERGY-ABSORPTION DIAGRAMS

The commonest use of foams is in packaging. The aim is to absorb energy (usually the kinetic energy) of the packaged object when it is dropped, or is accelerated or decelerated in some other way, while at the same time keeping the force on the object below the limit which will cause damage. In selecting a material for the package, we need to know the *energy* that can be absorbed without the *stress* exceeding a critical value. We show below that there is an optimum foam density for a given package. If the density is too low, the foam 'bottoms out' (with a sharp increase in stress) before enough energy has been absorbed. If

it is too dense, the stress exceeds the critical value before enough energy has been absorbed.

Figure 19 shows, inset, part of a stress-strain curve for a foam. It is linear-elastic to ϵ_0 , and thereafter follows the stress-strain $\sigma(\epsilon)$ curve described approximately by eqn. (17) or (18). The area, up to the strain ϵ^* , where the stress is σ , (shaded on Fig. 19) is:

$$W = \int_0^{\epsilon_0} \sigma d\epsilon + \int_{\epsilon_0}^{\epsilon^*} \sigma(\epsilon) d\epsilon$$

or

$$\frac{W}{E_s} = \frac{1}{2} \frac{E}{E_s} \epsilon_0^2 + \int_{\epsilon_0}^{\epsilon^*} \frac{\sigma(\epsilon)}{E_s} d\epsilon$$

This equation was integrated numerically, using eqn. (17) for $\sigma(\epsilon)$ for elastic foams and eqn. (18) for plastic foams, to give Figs. 19 and 21. Similar diagrams can, of course, be constructed directly from its experimental stress-strain curves (such as those shown in Figs. 3 to 6) by measuring the area W/E_s up to the strain ϵ^* corresponding to the stress σ/E_s . Such diagrams are shown, for comparison, in Figs. 20 and 22.

The energy diagram, calculated for elastic foams (Fig. 19) shows the normalised energy absorbed per unit volume of foam, W/E_s , plotted against the peak stress σ/E_s , for a range of densities ρ/ρ_s . Normalised in this way, the diagram describes all elastic foams. If the critical damage stress is selected, then the diagram gives the foam density which will absorb the greatest amount of energy without this stress being exceeded. The lower the peak stress, the lower is the optimum foam density. As an example, using Fig. 19 or 20, the optimum foam density for a critical damage stress $\sigma/E_s = 10^{-3}$ is $\rho/\rho_s = 0.1$. Choosing the right density is important: it can easily give a factor of 10 greater absorption of energy than a wrongly-chosen foam.

Figures 21 and 22 show energy diagrams for a plastic foam with $\sigma_y/E_s = 0.1$. Such diagrams are less general than those for elastic foams, because σ_y/E_s must be specified; but a single diagram still describes all foams made of a given material (polystyrene, for example). Here, too, there is an optimum foam density for a given energy absorption and peak stress. The diagram allows it to be chosen.

The figures show that, for a given material (and thus E_s), there is a maximum energy which can be absorbed for a given peak stress. The envelope shown as a broken line on Figs. 19 and 21 divides the diagram into an accessible region (below the line) and an inaccessible one (above). For elastomeric foams, the equation of the line is approximately:

$$W/E_s = 0.11 \left(\frac{\sigma}{E_s}\right)^{7/8}$$

It applies to all elastic foams. For the plastic foam with $\sigma_y/E_s = 0.1$, the equation of the line is approximately:

$$W/E_s = 0.05 \left(\frac{\sigma}{E_s}\right)^{2/3}$$

The equations from $\rho/\rho_s = 0.01$ to $\rho/\rho_s = 0.3$.

6. CONCLUSIONS AND APPLICATIONS

6.1 Conclusions

When a cellular solid with a relative density below 0.30 is compressed, it shows a stress-strain curve with three parts: a linear-elastic part, a long plateau, and a regime of final densification. The properties of an entire class of such solids can be summarised as a deformation-mode map, which shows how each of the three parts changes as the relative

density changes. The method can be applied to man-made foams (Figs. 13 to 16) and to natural materials, such as woods (Figs. 17 and 18), to give diagrams which summarise the stress-strain response of each class of material.

The mechanical properties of cellular solids can be modelled with precision. The models lead to constitutive laws (stress-strain relations) which have been thoroughly tested in simple compression. They are summarised in Table 4. The constitutive laws can be used to construct deformation-mode maps, and can be integrated to construct energy-absorption diagrams. These diagrams (Figs. 19 to 22) show how the energy absorbed, per unit volume of foam, depends on the density of the foam and on the stress. The diagrams show that there is an optimum foam density for a given packaging or energy-absorbing application.

6.2 Design with Cellular Solids

The equations derived in the text, and summarised in Table 4, provide the basic information for design with foams in load-bearing applications. The tests described above all involved simple compression. Under multiaxial loads, the behaviour is more complicated. At small strains ($\epsilon < 5\%$), while the material is linear-elastic, it behaves like any other elastic solid (1,3) with Young's modulus E^* given by eqn. (6) and Poisson's ratio $\nu = \frac{1}{3}$. But once the plateau-stress has been reached, the behaviour changes: the extensive deformation at nearly constant stress involves a large volume change, but almost no lateral strain (1,3,26,27) so that $\nu \approx 0$. Then the material deforms under a multiaxial state of stress when the maximum principal stress (not the octahedral shear stress) reaches the critical value σ^* (eqn. 8 for flexible foams, eqn. 10 for plastic foams). Because of this, the indentation

hardness of plastic foams is equal to σ_{pl}^* (not $3\sigma_{pl}^*$ as in dense solids) and the force needed to compress a foam is the same whether it is free at its edges or constrained there (15). Once densification starts, of course, the properties revert towards those of conventional solids.

The deformation mode map for a class of foams provides a compact summary of the mechanical response of the class. In particular, the maps give a rational way of selecting the material and density which will give a desired stress-strain response. Similarly, the energy-absorption diagram for a class of foam summarises the energy absorbing capacity of all members of the class. The diagrams identify the optimum foam material and density for a given packaging, padding or cushioning application.

Acknowledgements

We wish to thank Professor K.E. Easterling and Dr. C.R. Calladine for many helpful discussions. We particularly wish to thank Mr. John Godlonton for technical assistance and Trish Shepherd for typing the manuscript. Finally, we wish to acknowledge the support of the U.S. Army Research Office through a research contract.

TABLE 2: MATERIALS

MATERIAL	DENSITY RANGE kg/m ³	ρ_s (kg/m ³)	E _s (MPa)	σ_y (MPa)	σ_f (MPa)	SOURCE OF MATERIALS
Flexible Polyethylene	29-360	1200	700	-	-	"Frelen"
Flexible Polyurethane	14-52	1100	45	-	-	"Dunlopillo", Dunlop Ltd., G.B.
Styrene Acryllimid	34-186	1200	3600	360	-	"Rohacell", Rohm GmbH, W. Germany
Stable Mullite	100-320	3200	3600	-	4	Morgan Thermic Ltd., G.B.
Stable Mullite (axial compression)	103-787	1500	10000	135	-	Commercial suppliers of } seasoned woods
Stable Mullite (axial compression)	103-764	1500	35000	135	-	

TABLE 3: EXPERIMENTAL MEASUREMENTS

SAMPLE	ρ (kg/m ³)	E^* (MPa)		σ^* (MPa)
<u>ELASTOMERIC FOAMS</u>				
Dunlop D1	14.4		0.054	0.002
D14	32.4		0.062	0.0025
D17	51.7		0.057	0.005
Frelen F30	29.4		0.275	0.04
F70	69.2		1.10	0.1
F120	120.0		3.82	0.24
F175	138		4.58	0.3
F250	360		23.45	2.56
<u>PLASTIC FOAMS</u>				
		Tension	Compr.	
Rohacell 31	34	43	20.8	0.4
51	51.6	73.4	28.1	0.8
71	70.4	95.2	56.9	1.6
110	124	194	129.7	3.0
170	160	280	198.7	5.2
190	185.7	432	258.9	6.0
<u>BRITTLE FOAMS</u>				
S1	100		8-50	0.02 -0.18
S2	200		6-22	0.035-0.16
S3	280		2-8	0.072-0.21
S4	320		25-44	0.093-0.16
<u>WOODS</u>				
Balsa	103	103	31	420
Balsa	124	124	79	258
Willow	403	395	198	1270
Pine	443	-	647	-
Willow	520	385	321	2203
Mahogany	615	-	610	-
Beech	711	735	1160	7393
Beech	737	764	1569	7500
			Radial	Axial

TABLE 4: EQUATION FOR STIFFNESS AND STRENGTH OF CELLULAR SOLIDS

Property	Equation	Eqn. No.
Young's modulus	$\frac{E^*}{E_s} = \left(\frac{\rho}{\rho_s}\right)^2$	(6)
Plateau stress, flexible foams	$\frac{\sigma_{el}^*}{E_s} = 0.05 \left(\frac{\rho}{\rho_s}\right)^2$	(8)
Plateau stress, plastic foams	$\frac{\sigma_{pl}^*}{\sigma_y} = 0.3 \left(\frac{\rho}{\rho_s}\right)^{\frac{3}{2}}$	(10)
Approximate plateau stress, brittle foams	$\frac{\sigma_f^*}{\sigma_f} = 0.65 \left(\frac{\rho}{\rho_s}\right)^{\frac{3}{2}}$	(11)
Stress-strain response, flexible foam	$\frac{\sigma}{E_s} = 0.05 \left(\frac{\rho}{\rho_s}\right)^2 \left\{ \frac{1 - \left(\frac{\rho}{\rho_s}\right)^{\frac{1}{3}}}{1 - \left(\frac{\rho}{\rho_s} \left(\frac{1}{1-\epsilon} \right)\right)^{\frac{1}{3}}} \right\}^2$	(17)
Stress-strain response, plastic foam	$\frac{\sigma}{\sigma_y} = 0.3 \left(\frac{\rho}{\rho_s}\right)^{\frac{3}{2}} \left\{ \frac{1 - \left(\frac{\rho}{\rho_s}\right)^{\frac{1}{3}}}{1 - \left(\frac{\rho}{\rho_s} \left(\frac{1}{1-\epsilon} \right)\right)^{\frac{1}{3}}} \right\}$	(18)

REFERENCES

1. Gibson, L.J., Ph.D. Thesis, Engineering Department, Cambridge University, (1981).
2. Gibson, L.J., Ashby, M.F., Schajer, G.S. and Robertson, C.I., Proc. R. Soc. Lond. A382, 25, (1982).
3. Gibson, L.J. and Ashby, M.F., Proc. R. Soc. Lond. A382, 43, (1982).
4. Ashby, M.F., Met. Trans. 14A, 1755, (1983).
5. Patel, M.R. and Finnie, I., J. Materials 5, 909, (1970).
6. Ko, W.L., J. Cell. Plastics 1, 45, (1965).
7. Menges, G. and Knipschild, F., Polymer Eng. Sci. 15, 623, (1975).
8. Gent, A.N. and Thomas, A.G., J. Appl. Polymer Sci. 1, 107, (1959).
9. Lederman, J.M., J. Appl. Polymer Sci. 15, 693, (1971).
10. Baxter, S. and Jones, T.T., Plastics Polymers 40, 69, (1972).
11. Phillips, P.J. and Waterman, N.R., Polymer Eng. Sci. 4, 67, (1974).
12. Moore, D.R., "The use of glass in engineering", Design Council Guide 05, Oxford: University Press, (1980).
13. Chan, R. and Nakamura, M., J. Cell Plastics 5, 112, (1969).
14. Brighton, C.A. and Meazey, A.E., Expanded polyvinyl chloride. In "Expanded Plastics - Trends in Performance Requirements" - A Micro Symposium organized by Q.M.C. Industrial Research Ltd., September 25, (1973) London.
15. Wilsea, M., Johnson, K.L. and Ashby, M.F., Int. J. Mech. Sci. 17, 457, (1975).
16. Walsh, J.B., Brace, W.F. and England, A.W., J. Am. Ceram. Soc. 48, 605, (1965).
17. Pittsburgh-Corning Inc., Foamglass Data Sheets (1982).
18. Gent, A.M. and Thomas, A.G., Rubber Chem. Technol. 36, 597, (1963).
19. Thornton, P.H. and Magee, C.L., Met. Trans. 6A, 1253, (1975).
20. Thornton, P.H. and Magee, C.L., Met. Trans. 6A, 1801, (1975).
21. Traeger, R.K., J. Cell. Plastics 3, 405, (1967).
22. Matonis, V.A., Soc. Plas. Eng. J., Sept., 1024, (1964).

23. Rusch, K.C., J. Appl. Poly. Sci. 14, 1263, (1970).
24. McIntyre, A. and Anderton, G.E., Polymer 20, 247, (1979).
25. Fowlkes, C.W., Int. J. Fracture 10, 99, (1974).
26. Shaw, M.C. and Sata, T., Int. J. Mech. Sci. 8, 469, (1966).
27. Rinde, J.A., J. Appl. Poly. Sci. 14, 1913, (1970).
28. Maiti, S., Ashby, M.F. and Gibson, L.J., Scripta Met. ___, (1984).
29. Easterling, K.E., Harrysson, R., Gibson, L.J. and Ashby, M.F., Proc. R. Soc. Lond. A383, 31, (1982).
30. Dinwoodie, J.M., "Timber: Its Nature and Behaviour", New York, Van Nostrand (1981).

FIGURE CAPTIONS

- Fig. 1. Schematic of cellular material, showing dimensions.
- Fig. 2. Microstructures of the four types of foam:
 (a) polyethylene $\rho/\rho_s = 0.115$; (b) polyurethane $\rho/\rho_s = 0.029$;
 (c) polymethylacrylimide $\rho/\rho_s = 0.103$; (d) mullite $\rho/\rho_s = 0.062$.
- Fig. 3. Compressive stress-strain curves for flexible polyethylene foams.
- Fig. 4. Compressive stress-strain curves for flexible polyurethane foams.
- Fig. 5. Compressive stress-strain curves for rigid (plastic) polymethylacrylimid foams.
- Fig. 6. Compressive stress-strain curve for a brittle mullite foam.
- Fig. 7. Compressive stress-strain curves for woods, in the radial direction (perpendicular to the grain).
- Fig. 8. Compressive stress-strain curves for woods in the axial direction (parallel to the grain).
- Fig. 9. The relative Young's modulus, E^*/E_s , plotted against relative density. ρ/ρ_s .
- Fig. 10. The relative elastic collapse stress, σ_{el}^*/E_s , plotted against relative density, ρ/ρ_s .
- Fig. 11. The relative plastic collapse stress, σ_{pl}^*/σ_y , plotted against relative density ρ/ρ_s .
- Fig. 12. The relative crushing strength, σ_f^*/σ_f , plotted against relative density ρ/ρ_s , for brittle foams.
- Fig. 13. A deformation mode map for flexible foams. It shows the data of Figs. 4 and 5, normalised. The construction of the field boundaries is described in the text.

Fig. 14. A deformation-mode map for flexible foams, constructed entirely from the equations developed in the text.

Fig. 15. A deformation-mode map for plastic foams. It shows the data of Fig. 6, normalised. The construction of the field boundaries is described in the text.

Fig. 16. A deformation-mode map for plastic foams, constructed entirely from the equations developed in the text.

Fig. 17. A deformation-mode map for woods, tested in the radial direction (across the grain).

Fig. 18. A deformation-mode map for woods tested in the axial direction (along the grain).

Fig. 19. An energy-absorption diagram for elastomeric foams, constructed from the equations given in the text. The broken line divides the diagram into an accessible and an inaccessible region.

Fig. 20. An energy-absorption diagram for elastomeric foams, constructed by measuring the areas under the stress-strain curves of Figs. 3 and 4. It is directly comparable with Fig. 19.

Fig. 21. An energy-absorption diagram for plastic foams, constructed from the equations given in the text, with $\sigma_y/E_s = 0.1$. The broken line divides the diagram into an accessible and an inaccessible region.

Fig. 22. An energy-absorption diagram for polymethacrylimid foams, constructed by measuring the areas under the stress-strain curves of Fig. 5. It is directly comparable with Fig. 21.

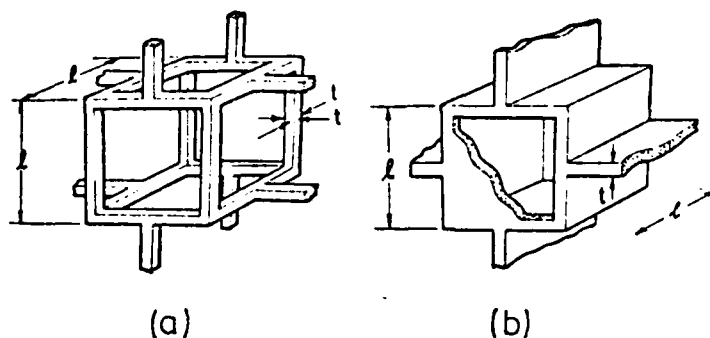


Fig. 1. Schematic of cellular material, showing dimensions.

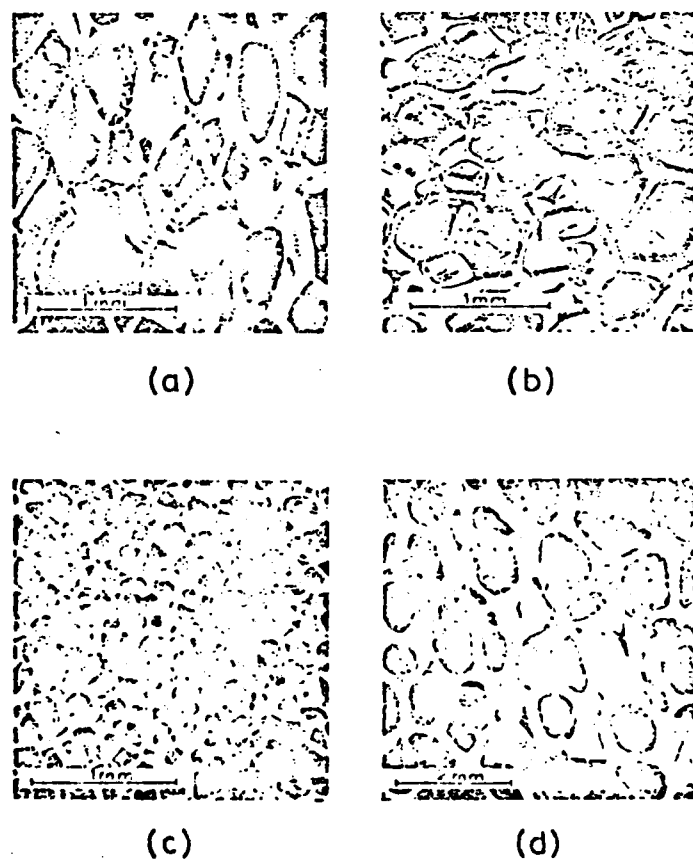


Fig. 2. Microstructures of the four types of foam:

- (a) polyethylene $\rho/\rho_s = 0.115$; (b) polyurethane $\rho/\rho_s = 0.029$;
- (c) polymethylacrylimide $\rho/\rho_s = 0.103$; (d) mullite $\rho/\rho_s = 0.062$.

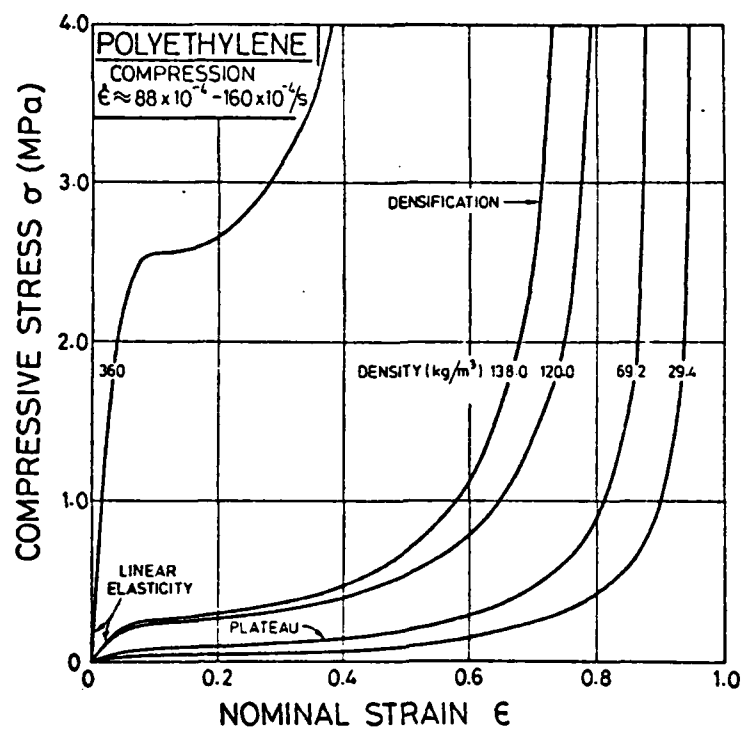


Fig. 3. Compressive stress-strain curves for flexible polyethylene foams.

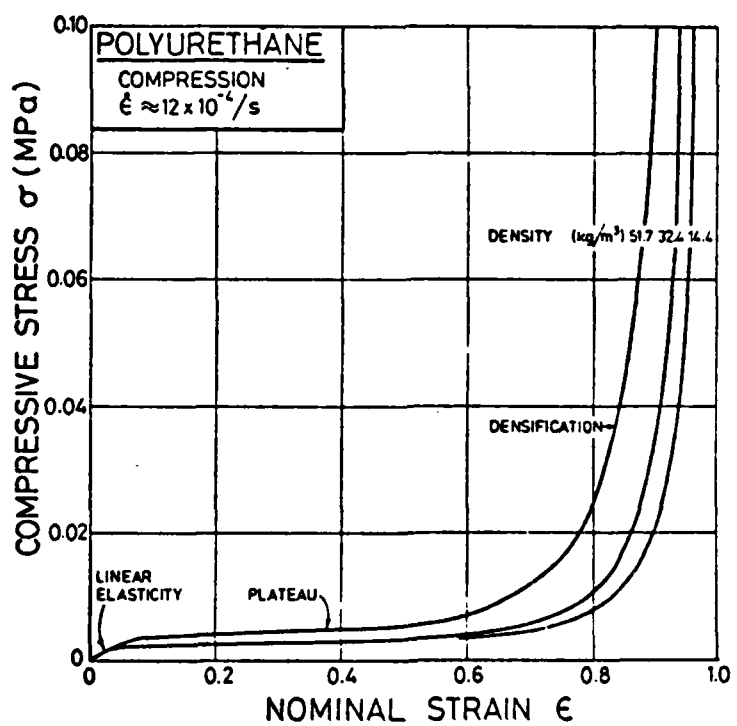


Fig. 4. Compressive stress-strain curves for flexible polyurethane foams.

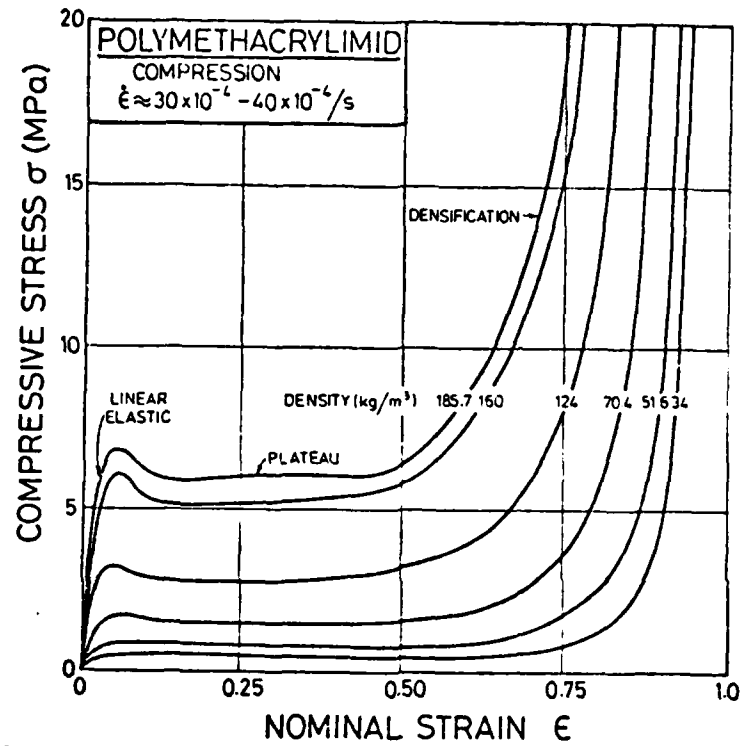


Fig. 5. Compressive stress-strain curves for rigid (plastic) polymethylacrylimid foams.

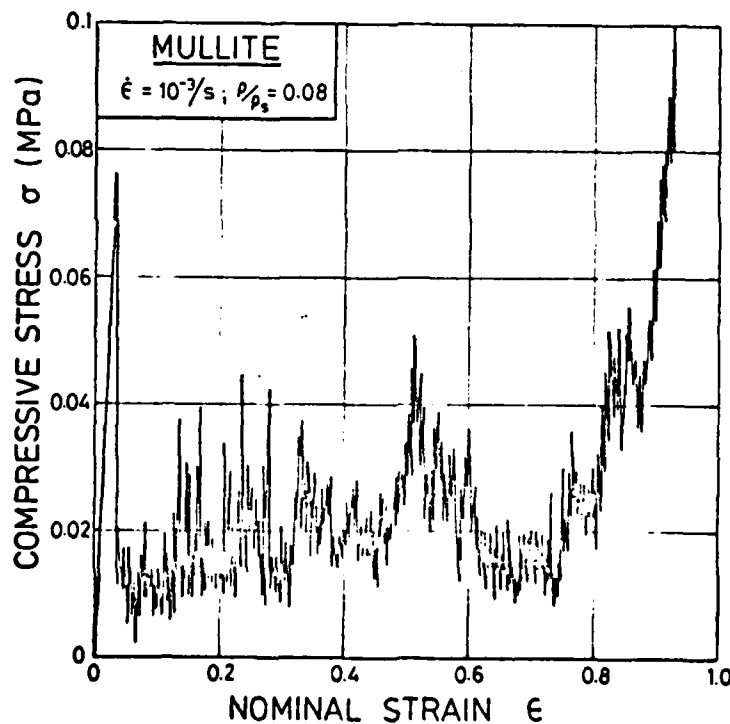


Fig. 6. Compressive stress-strain curve for a brittle mullite foam.

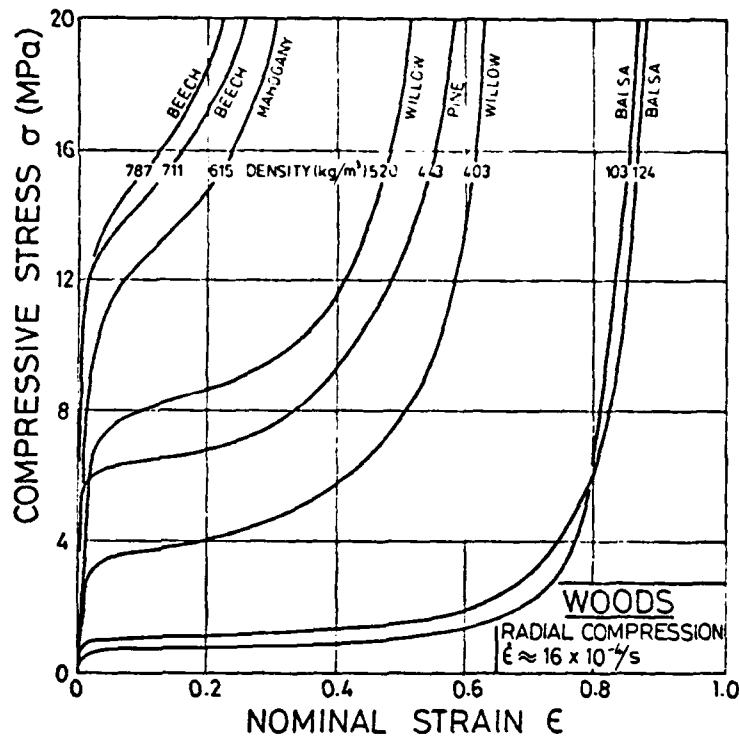


Fig. 7. Compressive stress-strain curves for woods, in the radial direction (perpendicular to the grain).

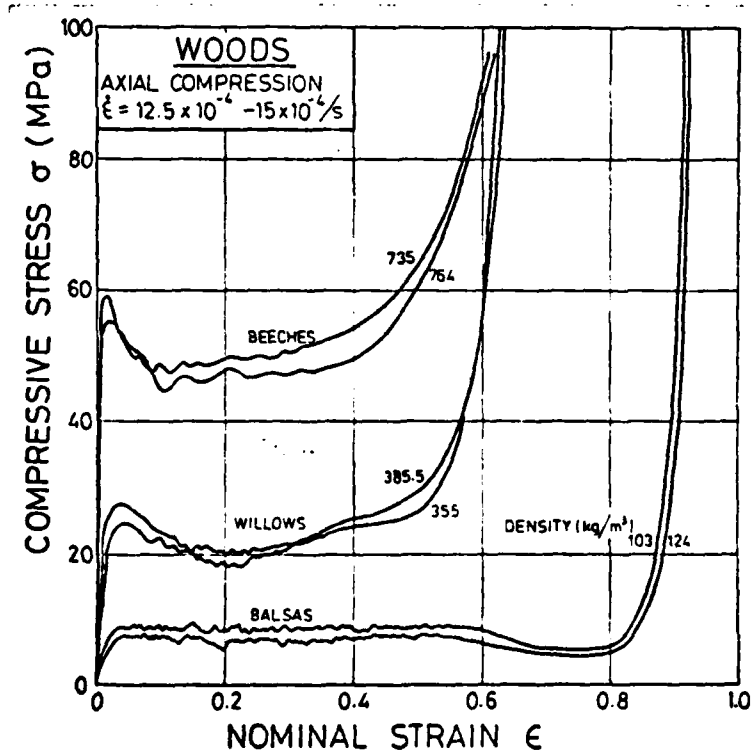


Fig. 8. Compressive stress-strain curves for woods in the axial direction (parallel to the grain).

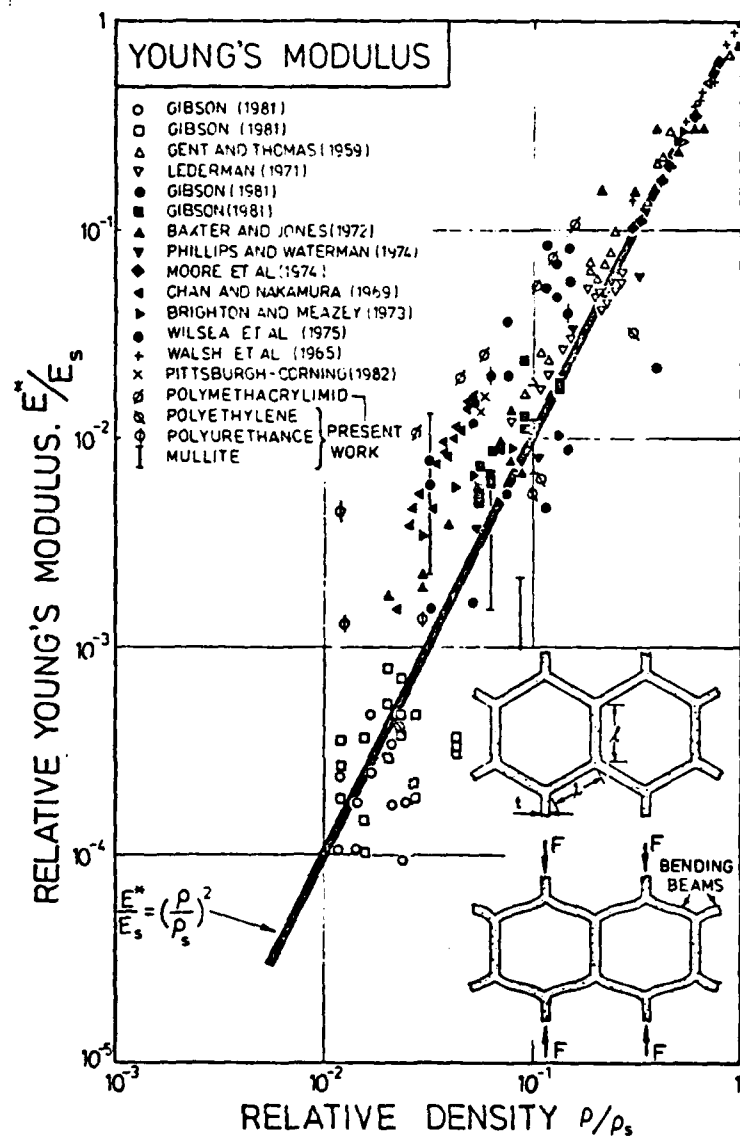


Fig. 9. The relative Young's modulus, E^*/E_s , plotted against relative density. ρ/ρ_s .

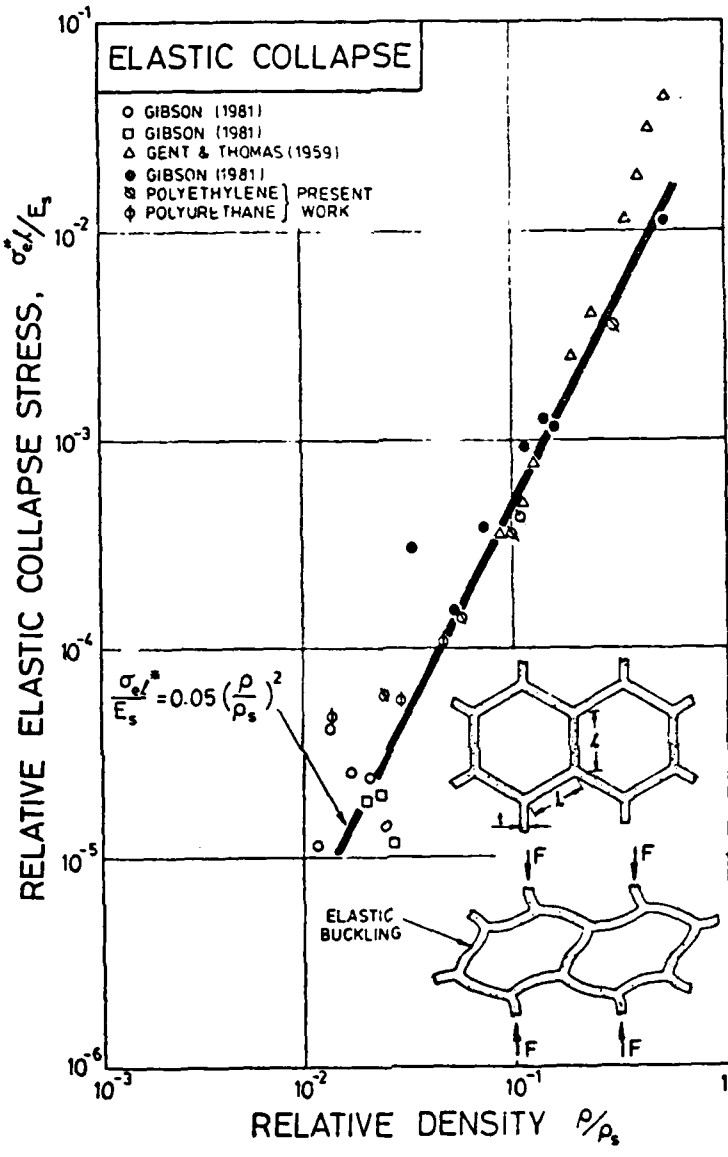


Fig. 10. The relative elastic collapse stress, σ_{el}^*/E_s , plotted against relative density, ρ/ρ_s .

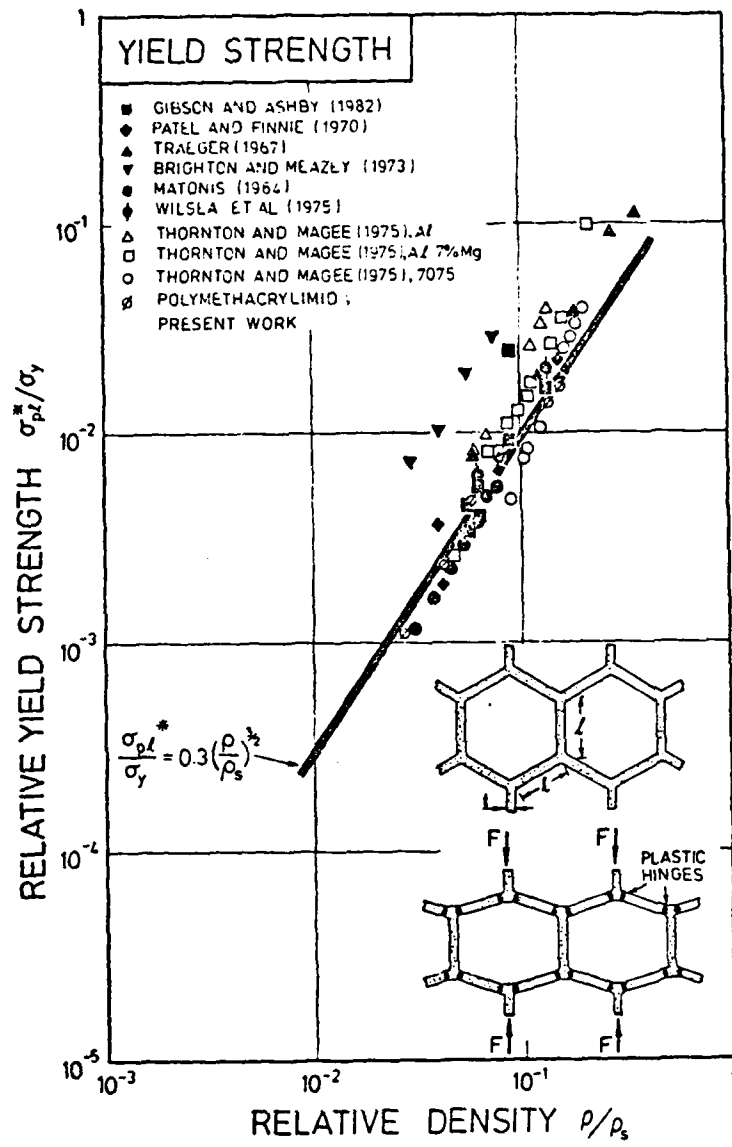


Fig. 11. The relative plastic collapse stress, σ_{pl}^*/σ_y , plotted against relative density ρ/ρ_s .

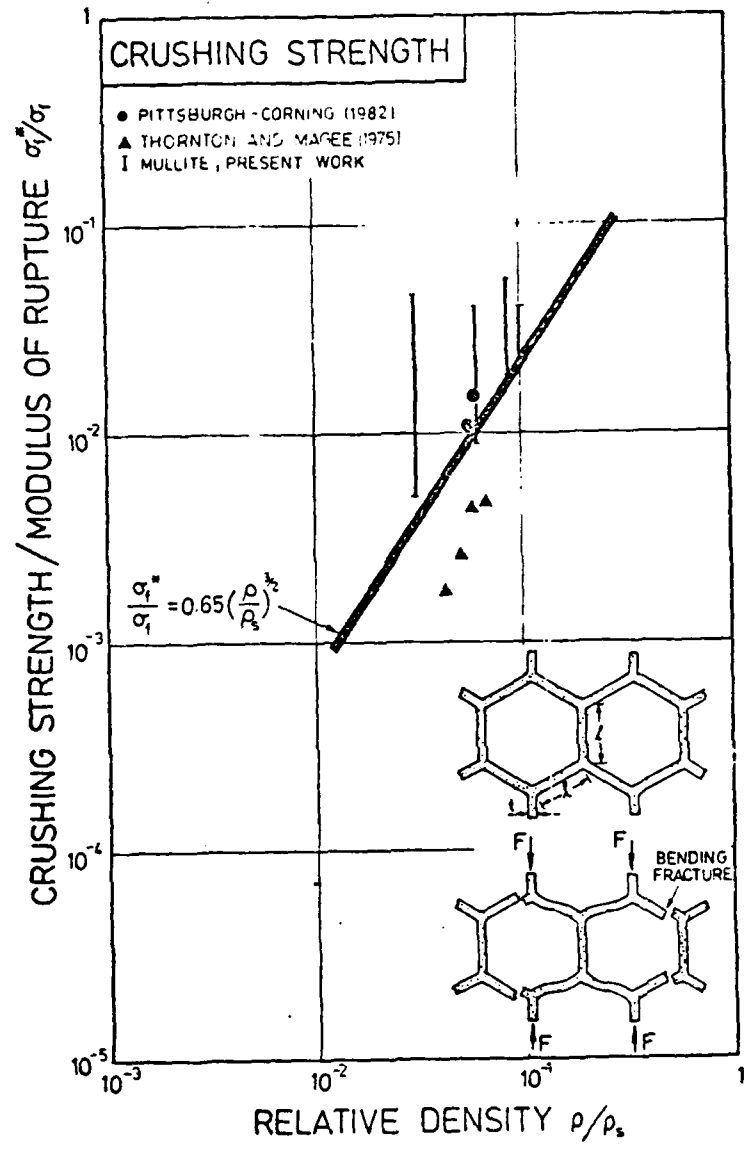


Fig. 12. The relative crushing strength, σ_f^*/σ_f , plotted against relative density ρ/ρ_s , for brittle foams.

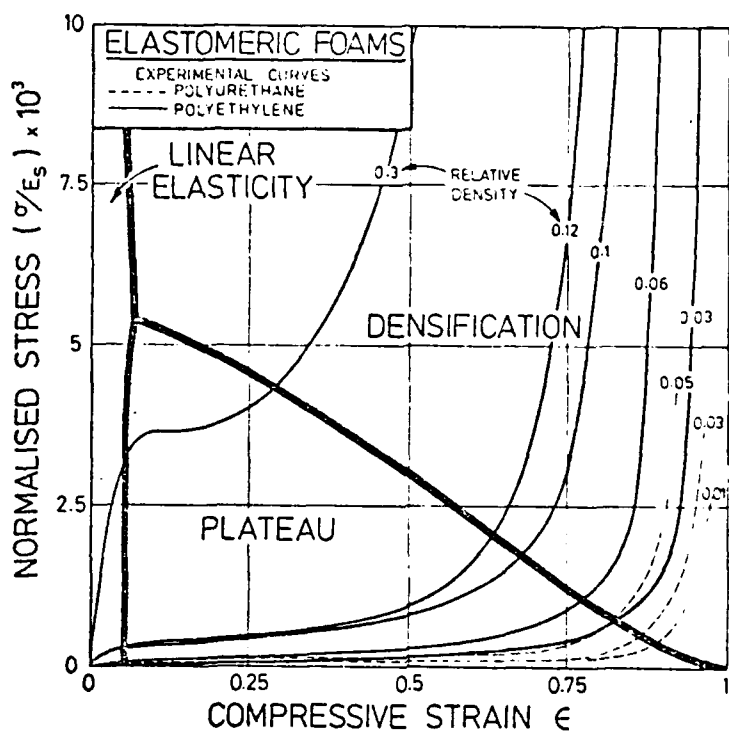


Fig. 13. A deformation mode map for flexible foams. It shows the data of Figs. 4 and 5, normalised. The construction of the field boundaries is described in the text.

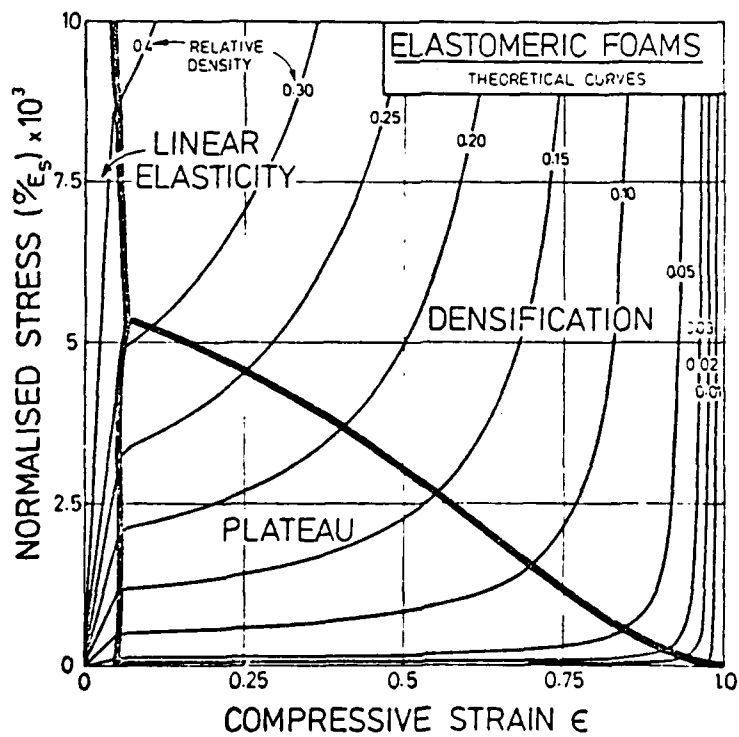


Fig. 14. A deformation-mode map for flexible foams, constructed entirely from the equations developed in the text.

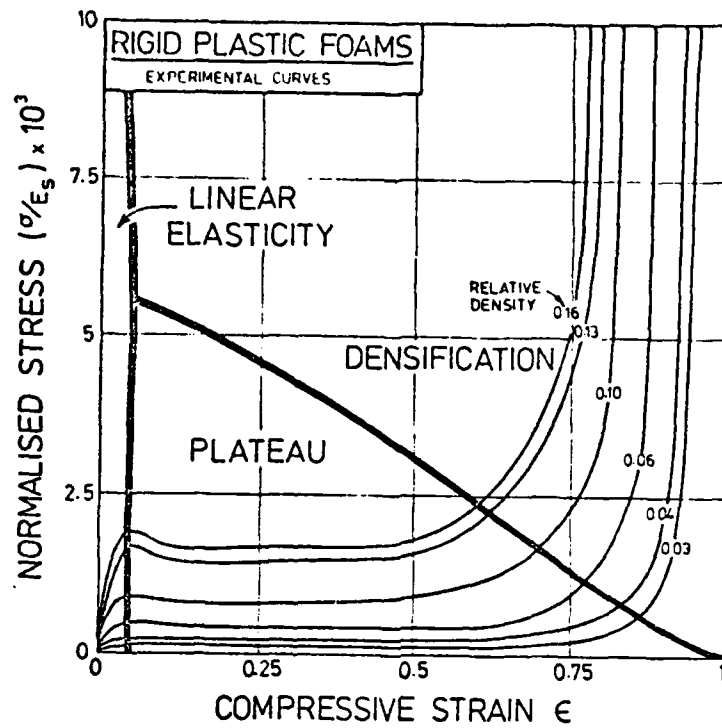


Fig. 15. A deformation-mode map for plastic foams. It shows the data of Fig. 6, normalised. The construction of the field boundaries is described in the text.

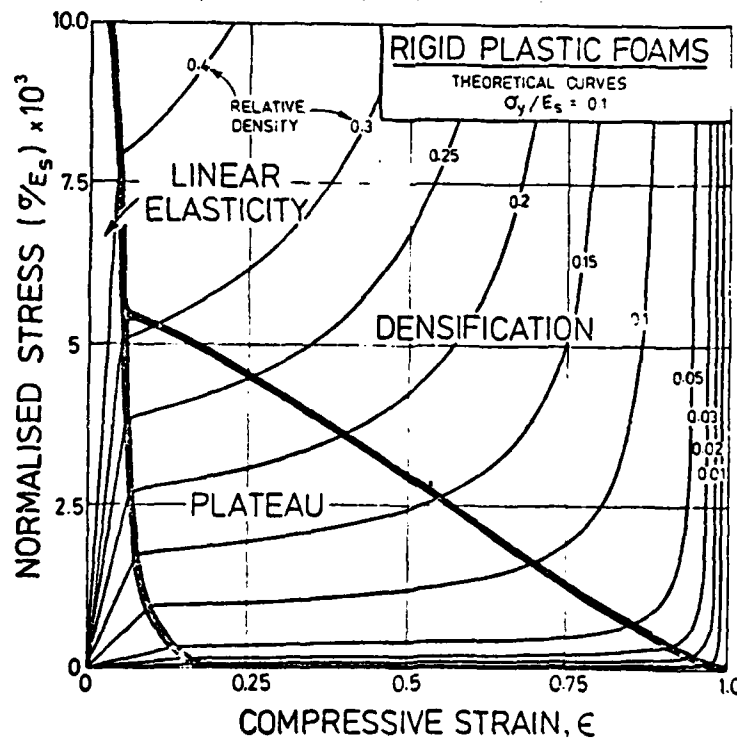


Fig. 16. A deformation-mode map for plastic foams, constructed entirely from the equations developed in the text.

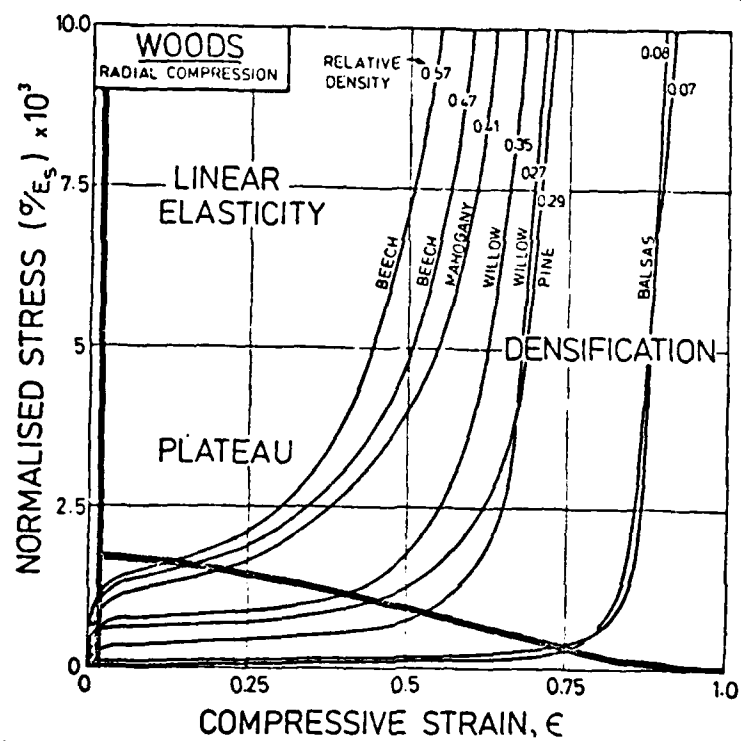


Fig. 17. A deformation-mode map for woods, tested in the radial direction (across the grain).

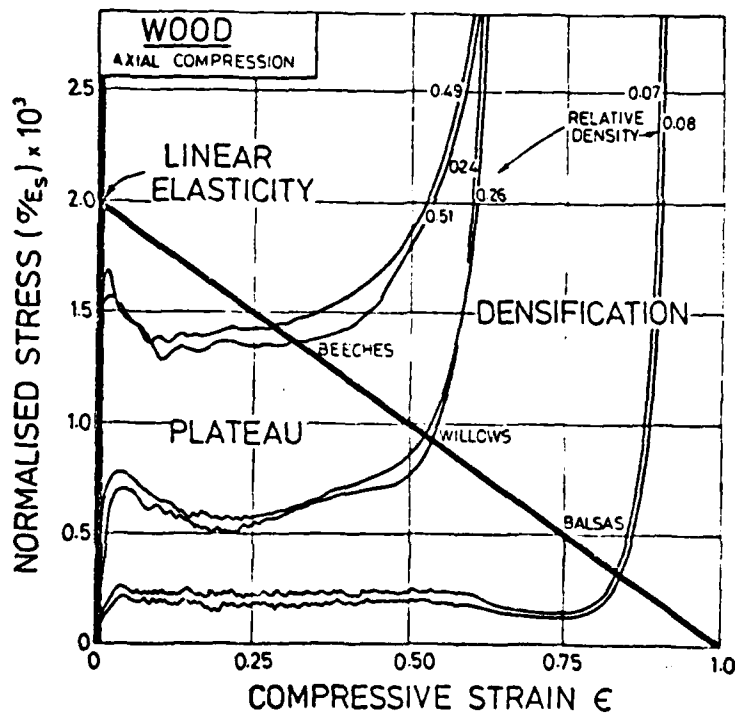


Fig. 18. A deformation-mode map for woods tested in the axial direction (along the grain).

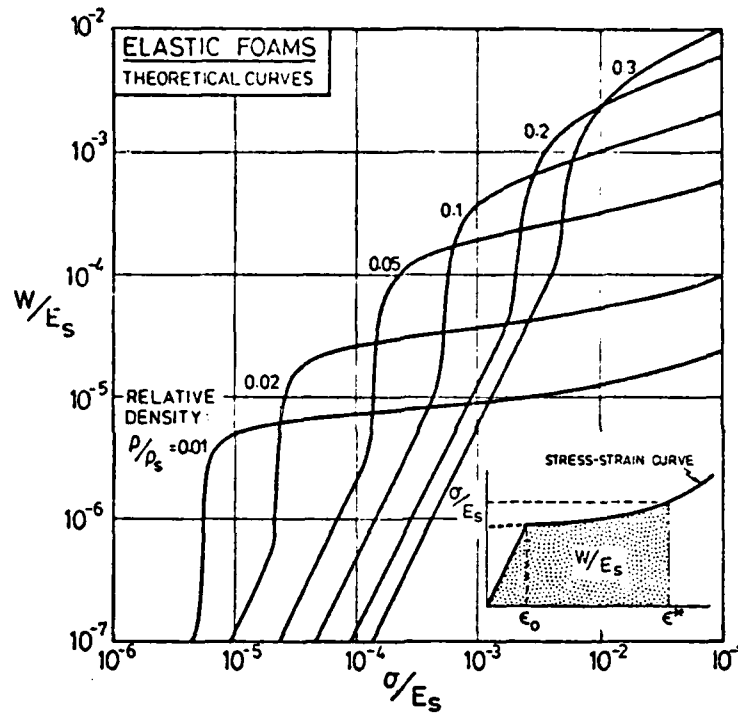


Fig. 19. An energy-absorption diagram for elastomeric foams, constructed from the equations given in the text. The broken line divides the diagram into an accessible and an inaccessible region.

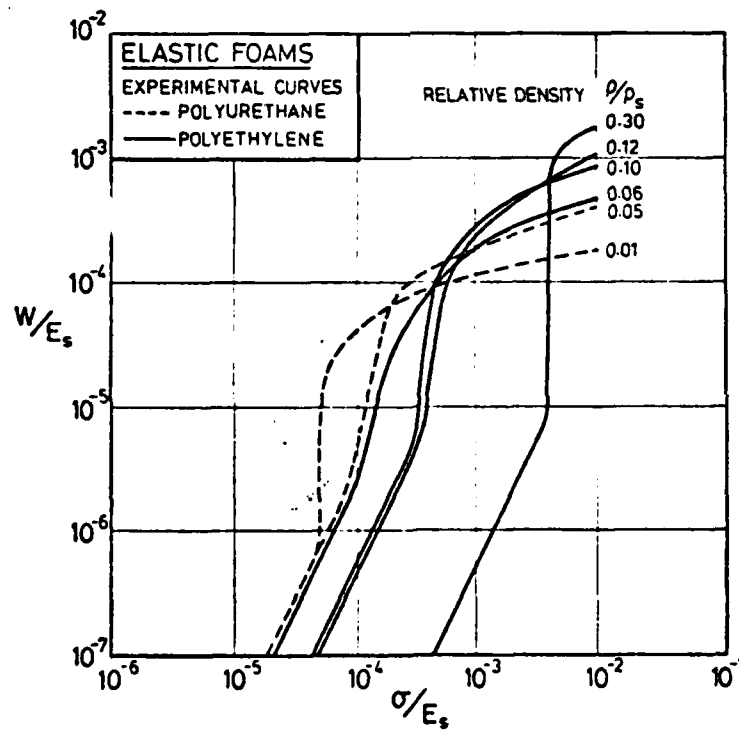


Fig. 20. An energy-absorption diagram for elastomeric foams, constructed by measuring the areas under the stress-strain curves of Figs. 3 and 4. It is directly comparable with Fig. 19.

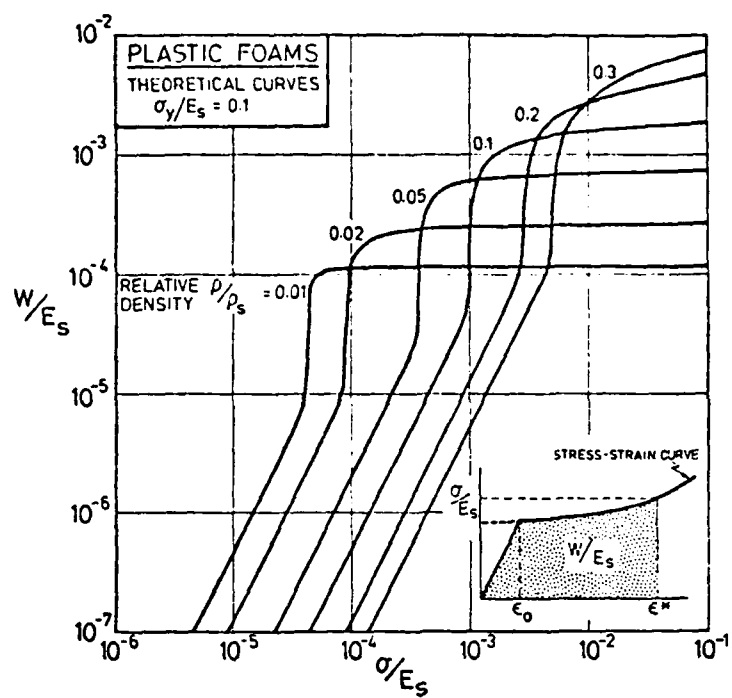


Fig. 21. An energy-absorption diagram for plastic foams, constructed from the equations given in the text, with $\sigma_y/E_s = 0.1$. The broken line divides the diagram into an accessible and an inaccessible region.

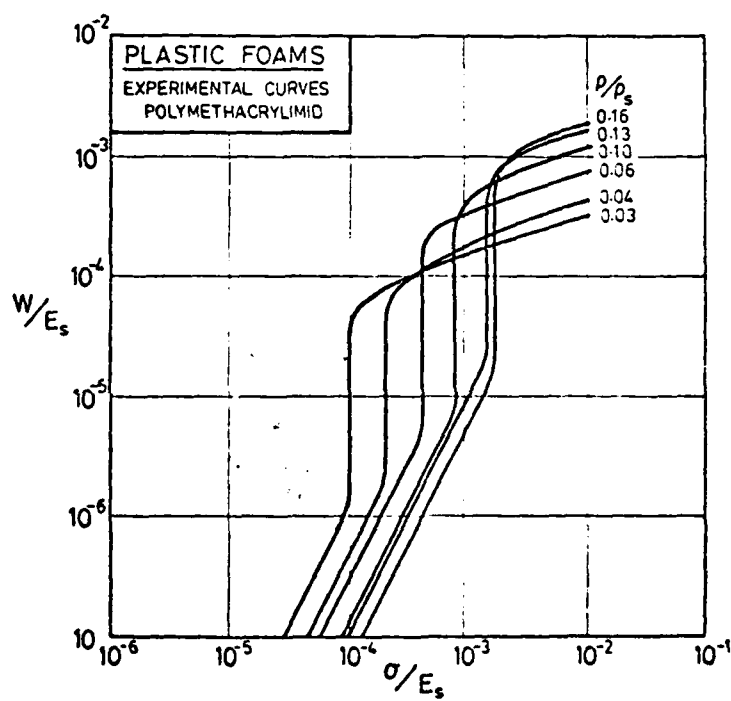


Fig. 22. An energy-absorption diagram for polymethacrylimid foams, constructed by measuring the areas under the stress-strain curves of Fig. 5. It is directly comparable with Fig. 21.

DEFORMATION MAPS FOR AMORPHOUS POLYMERS

D.G. Gilbert, M.F. Ashby and P.W.R. Beaumont

Cambridge University, Engineering Dept.,
Trumpington Street, Cambridge CB2 1PZ, U.K.

ABSTRACT

This paper explores the possibility of constructing deformation-mechanism maps for amorphous polymers. Five regimes are identified: the glassy regime, the visco-elastic regime, the rubbery regime and the regime of viscous flow (melting), truncated by decomposition. Constitutive equations for each regime are assembled and adapted to give a good description of a large body of experimental data for amorphous polymethylmethacrylate and polystyrene. The adjusted laws are then used to construct diagrams which relate the time- and temperature-dependent modulus, $E(t,T)$, to the temperature and the loading time (or frequency). The diagrams are divided into fields corresponding to the five regimes. A diagram summarises the small-strain mechanical behaviour of the polymer over a wide range of conditions.

TABLE 1: SYMBOLS, DEFINITIONS AND UNITS

T	Temperature (K)
σ	Tensile or compressive stress (MPa)
ϵ	Tensile or compressive strain
$\dot{\epsilon}$	Tensile or compressive strain rate (s^{-1})
t	Time (s)
v	Frequency (s^{-1})
E	Time and temperature dependent Young's modulus (MPa)
E_0	Modulus at 0 K (MPa)
α_m	Temperature coefficient of modulus
T_g	Glass temperature (K)
T_D	Depolymerisation temperature
\bar{M}_w , M_{cr} , \bar{M}_e	Molecular weights (kg/mol)
Q_m	Mean activation energy (kJ/mol)
$\Delta Q/Q_m$	Fractional standard deviation of activation energy
$\Delta E/E_0$	Fractional modulus drop at a transition
a_T	Shift factor for time-temperature-equivalence
η	Viscosity (Ns/m^2)
η_0	Pre-exponential for viscosity (Ns/m^2)
α_g , α_v	Bulk thermal expansion coefficient below and above T_g (K^{-1})
C_1 , C_2	W.L.F. constants (see eqn. 15)
ρ	Density (kg/m^3)
f	Fractional free volume
V	Internal energy per unit volume (J/m^3)
R	Gas constant (8.314 J/mol K)
E_v	Energy of formation of vacancies in a crystal (J/mol)
E_j	Energy of motion of vacancies in a crystal (J/mol)
v_0	A pre-exponential frequency factor (s^{-1})

1. INTRODUCTION

GAB1, Disc 8

When a polymer is loaded, it suffers deformation which, in general, increases with time of loading. For uniaxial loading, the resistance to small-strain deformation is conventionally measured by the time-and temperature-dependent modulus, $E(t, T)$ (from now on simply called E). If, for instance, a constant stress σ is applied to a sample of the polymer, giving a strain $\epsilon(t, T)$ after a time t at temperature T , then:

$$E = \frac{\sigma}{\epsilon(t, T)} \quad (1)$$

Linear amorphous polymers like polymethylmethacrylate (PMMA) or polystyrene (PS) show five distinct regimes of deformation, in each of which the modulus has certain characteristics, illustrated in Fig. 1.

- (a) The glassy regime, with a modulus of between 1 and 10 GPa, associated with stretching and bending of intermolecular bonds, and showing only a slight time dependence associated with a number of secondary relaxations.
- .
- (b) The glass-transition regime, in which the modulus drops steeply from around 1 GPa to near 1 MPa with increasing temperature or time of loading.
- (c) The rubbery regime, with a modulus of between 1 and 10 MPa, associated with the rubber-like sliding of the long-chain network of molecules, constrained by entanglements which behave (physically) like cross-links.
- (d) The viscous regime, at temperatures well above the glass transition temperature, in which the polymer can be thought of as a viscous liquid; its molecules move relative to each in a snake-like manner (reptation) which, when biased by stress, leads to viscous flow.
- (e) A regime of decomposition in which chemical breakdown begins.

Each regime is associated with a certain range of modulus. Each has been studied and modelled in more or less detail, and constitutive laws for each have been formulated - they are reviewed below. Experimental data for E , in each, are available for PMMA and PS. Our aim

here is to fit the constitutive laws to the data (requiring some modification to the models) and to examine how the laws can be combined to give a self-consistent description of small-strain deformation from 0 °K to above the melting temperature, and for all practical loading times. The results are assembled into diagrams which summarize the small-strain deformation behaviour of each polymer as a function of temperature, time and frequency.

We now examine the five regimes in more detail, reviewing, and selecting, among the constitutive laws for each. Symbols and their definitions are listed Table 1.

2. DEFORMATION MECHANISMS

The Glassy Regime and the α , γ and δ Relaxations

Well below the glass temperature, T_g , linear amorphous polymers have Young's moduli of, very roughly, 3 GPa. This is a direct reflection of the low-stiffness Van der Waals bonds which bind one chain to another as shown as dotted lines in Fig. 2: when the polymer is deformed, it is these bonds which stretch and bend. The covalent C-C bonds which form the chain backbone (full lines) are about 100 times stiffer than the Van der Waals bonds, and their stretching and bending contributes nothing significant to the elastic deformation. Rotation about a C-C bond is another matter: the single C-C bond rotates so easily that it is problems of steric hindrance, and thus the Van der Waals bonds, again, which limit its extent (Bowden, 1968; Yannas, 1974; Yannas and Luise, 1982).

If the internal energy of the polymer, per unit volume, is $V(\epsilon)$, then the glassy modulus at 0 K is calculated (in principle) by forming the second derivative of $V(\epsilon)$ with respect to ϵ :

$$E = - \frac{d^2 V(\epsilon)}{d\epsilon^2} \quad (2)$$

The difficulty is that of modelling $V(\epsilon)$ with enough precision to give more than an order-of-magnitude estimate of the modulus. To do so requires a potential function describing the Van der Waals bonds. Part of the elastic strain comes from bond stretching; then, commonly, a Lennard-Jones potential is summed over all molecules to give $V(\epsilon)$. Strain can also

result from rotation of segments of a single molecule about a C-C bond such a way that the molecule changes shape, (Bowden, 1968; Yannis, 1974). Then a potential which includes steric hindrance (Flory, 1969) must be used to calculate $V(\epsilon)$. But the fundamental understanding of intermolecular bonding in polymers is still too poor to allow $V(\epsilon)$ to be computed accurately from first principles in either case (in practice, experimental data for E are used to calibrate the potential functions, rather than the other way round). Instead, the modulus at absolute zero, E_0 , is obtained by extrapolating experimental measurements of E at slightly higher temperatures to absolute zero. It, and other material properties, are listed in Table 2.

Increasing the temperature has two distinct effects. First, thermal expansion increases the molecular separation and lowers the Van der Waals restoring forces: this gives a slow drop in modulus, but does not introduce a time or frequency-dependence. Second, the thermal energy of the molecules permits thermally-activated local rearrangements (usually, rotations about a C-C bond), giving time-dependent strain and an associated drop in modulus.

The first effect leads to a roughly linear decrease in modulus with increasing temperature. Yannas and Luise (1982) develop this idea: thermal expansion increases the inter-chain distance, reducing the force required for intermolecular deformation by bond stretching. The final form of their equation is cumbersome but simplifies to a linear relationship at low temperatures. Van Krevelen (1976) prefers the empirical relation:

$$E = E_0 / (1 + 2 T/T_g)$$

which, of course, is linear at low temperatures, but drops faster near T_g . In this paper we use a linear temperature dependence:

$$E = E_0 \left(1 - \alpha_m \frac{T}{T_g}\right) \quad (3)$$

to describe the drop in modulus caused by thermal expansion. The dimensionless coefficients α_m which best described the low temperature data for each polymer are listed in Table 2.

The second contribution comes from the small thermally-activated

rearrangements of side groups or short segments of chain at "loose sites" in the amorphous structure (Fig. 3). These relaxation processes, all occurring at temperatures below T_g (and known, in order of decreasing temperature, as the β , γ and δ relaxations) give additional strain, and they thereby reduce the modulus a little. Each relaxation is positioned for a given loading time or frequency, about a characteristic temperature at which thermal energy becomes sufficient to activate the rearrangement.

Like similar relaxations in crystalline solids, the response of the material to load is conveniently described by a rheological model. The simplest that is of any real use is the standard linear solid (Fig. 4a), composed of two springs of modulus E and ΔE , and a dashpot of viscosity:

$$\eta = \eta_0 \exp \frac{Q}{RT} \quad (4)$$

where Q is the activation energy for the process, R the gas constant and η_0 a constant which is chosen to fix the position of the drop in modulus. The standard-linear model gives a good phenomenological description of most anelastic relaxations in crystals, and relaxations in glasses do, very roughly, have the same characteristics. But more careful examination of data for amorphous polymers shows that the standard linear solid is too simple. Its response leads to an almost step like drop in modulus at the characteristic temperature; the real relaxation is broader (Fig. 5). This is no surprise. In PMMA, for instance, the β -relaxation is thought to be caused by a motion of the ester side-group, the γ -relaxation by the motion of one of the two methyl groups and the δ -relaxation by the motion of the other one (Fig. 3). The amorphous chain-packing grips some of these more tightly than others, so that each relaxation has a spectrum of activation energies. The response is then more realistically described by the parallel coupling of springs-and-dashpot units shown in Fig. 4(b), each dashpot describing a part of the activation energy spectrum.

This arrangement of units, rather than a more general one involving units in series and parallel, is justified in the following way. Relaxation involves the motion of isolated side groups - those which, at a given instant, are less tightly gripped than the rest. Each can be thought of as a small spherical volume in which viscous deformation takes place, embedded in an elastic matrix. The constitutive equation for a material consisting of viscous inclusions in an elastic matrix is discussed by Brown (1982): provided the dispersion of viscous spheres is dilute (meaning that they are well separated), the

material behaves like a standard linear solid (as in Fig. 4a). If each of the spherical volumes has a different activation energy (as is the case for the side-group relaxations discussed here) the same reasoning leads to the conclusions that the material behaves in a way described by Maxwell elements in parallel, as in Fig. 4b.

As explained, the spectrum of activation energies arises from differences in local packing density which makes it harder to move some side-groups than others. We have used a Gaussian distribution of activation energies with a mean Q_m and a standard deviation ΔQ . The proportion of units (that is, the fraction of the spheres) which relax with activation energies between Q and dQ is $f(Q)dQ$ where:

$$f(Q) = \frac{1}{\sqrt{2\pi}} \exp - \frac{1}{2} \left(\frac{Q - Q_m}{\Delta Q} \right)^2 \quad (5)$$

This defines a weighting function for each unit (Fig. 6) so that the modulus drop δE_i associated with full relaxation of the i^{th} unit is:

$$\delta E_i = \Delta E f(Q) dQ \quad (6)$$

where ΔE is the total modulus drop associated with the relaxation. This method introduces only one new variable, the standard deviation, ΔQ , into the calculation of the relaxation; it is chosen so that the width of the relaxation (Fig. 5) matches experiment. Data for ΔE , Q_m and $\Delta Q/Q_m$ PMMA and PS are listed in Table 2.

The Glass-Rubber Transition (The Visco-Elastic Regime)

As the temperature is raised, the Van der Waals bonds start to melt. Then segments of the previously elastically-bonded chains undergo larger sliding movements relative to each other and the material behaves in a visco-elastic way. Within this regime it is found that the modulus E at one temperature can be related to that at another by a change in the time scale only, that is, there is an equivalence between time and temperature. This means that the curve describing the modulus at one temperature can be

superimposed on that for another by a constant horizontal displacement $\log(a_T)$ along the $\log(t)$ or $\log(v)$ axis, as shown in Fig. 7.

In crystalline solids (notably metals) the time-temperature equivalence for the rate of diffusion, for creep, and for other thermally activated processes, is well known. The explanation is straight forward. Take diffusion as an example. The frequency with which an atom jumps from one lattice site to the next depends on the product of two probabilities: the probability $p_1 = \exp - (E_j/RT)$ that the diffusing atom has enough energy to clear the barrier (height E_j) which separates the two sites; and the probability $p_2 = \exp - (E_v/RT)$ that the second site is vacant, since if it is occupied the jumping atom cannot enter it. The jump frequency is then:

$$v = v_o \exp - \left(\frac{E_j}{RT} \right) \exp - \left(\frac{E_v}{RT} \right) = v_o \exp - \left(\frac{Q}{RT} \right) \quad (7)$$

where $Q = E_j + E_v$ is the activation energy for the process, and v_o is the atomic vibration frequency times various entropic and geometric terms which don't affect the argument. A change of temperature from T_1 to T_2 causes a change in frequency from v_1 to v_2 , where:

$$\log \left(\frac{v_1}{v_2} \right) = \log a_T = \frac{Q}{2.3 R} \left\{ \frac{1}{T_2} - \frac{1}{T_1} \right\} \quad (8)$$

A simple shift along the frequency or time axis by $\log(a_T)$ then brings the response at T_1 into coincidence with that at T_2 . This particular time-temperature equivalence is a consequence of the operation of a simple thermally-activated process with a single activation energy.

A spectrum of activation energies (which is inevitable in an amorphous system) does not destroy the time-temperature equivalence though it may change its form. If the width of the spectrum, ΔQ , is small (so that $\Delta Q \gg RT$) then it is easily shown that the shift factor defined by eqn. (8) still applies, and the relaxation follows simple Arrhenius kinetics. The α , γ and δ relaxations do, in fact, give linear Arrhenius plots; those for PMMA and PS are shown later. But the α , or glass-rubber transition is more complicated. Experiments on liquids and on amorphous polymers (Williams et al., 1955) are not well described by eqn. (8); they suggest,

instead, a shift factor (the "WLF" shift factor) given by:

$$\log a_T = \frac{C_1 (T - T_g)}{C_2 + T - T_g} \quad (9)$$

where C_1 and C_2 are constants (the "WLF" constants, with T_g as reference temperature). In the limit $T \gg C_2 - T_g$, this reduces to the simpler eqn. (8) with $C_1 = Q/2.3 RT_g$. But the values of C_2 are such that this is never a satisfactory approximation and a new, broader, physical interpretation must be sought.

The quest had produced a number of models (for brief reviews, see Ward, 1971; Arridge, 1975; Young, 1981). From these the following simplified picture can be assembled and related to the classical treatment of thermally activated processes in crystals just described. Viscous chain motion is caused by the stress-biased diffusion of polymer chains within the tubes which define their surroundings, as shown in Fig. 8. This snake-like diffusive motion, or "reptation", must involve the propagation of compression or shear wave pulses or kinks along the chain: in either case, the projecting side groups of one chain must move over and past those with which they mesh in the surrounding tube, as shown in Fig. 9.

The frequency of the unit step associated with producing viscous strain depends, as before, on the product of two probabilities: the probability p_1 that unit segments of the polymer chain have enough thermal energy to jump over the energy barrier which separates them from an adjacent position; and the probability p_2 that this second site is "vacant", i.e. that it has sufficient unoccupied volume associated with it to accommodate the jumping segment. The first probability, p_1 , is given by an Arrhenius law like eqn. (7). The second probability, p_2 , is more complicated. In crystals, unoccupied or "free" volume is quantized as vacancies of fixed volume. Free volume exists in amorphous systems too, but it is obviously not quantized in the way it is crystals. When the specific volume of an amorphous polymer is plotted against temperature (Fig. 10) there is a change of slope at T_g . The free volume (Cohen and Turnbull, 1959; Haward, 1973) is the difference between the total volume, V , and that occupied by the molecules themselves, V_o . The occupied volume is that of a dense (though disordered) packing of cylinders, one surrounding each chain, with a radius equal to the Van der Waals radius plus that associated with the local thermal vibrations of the atoms. What is left over is "free" in the sense that it ca.

redistribute continuously. Instead of a thermal-equilibrium concentration of vacancies, each of fixed volume, which move around continuously, the free volume exists (in thermal equilibrium, of course) as a spectrum of void volumes which continuously open up and close again. The thermal expansion data show that (unlike crystals) the free volume increases linearly with temperature. Defining the fractional free volume as:

$$f_v = \frac{V - V_0}{V} \quad (10)$$

we have that:

$$f_v = f_g + \alpha_f (T - T_g) \quad (11)$$

where f_g is the fractional free volume at the glass temperature. The quantity α_f is the free-volume expansion coefficient: it is the difference between the total expansion coefficient and that for the occupied volume. The figure shows how the value of α_f changes at T_g ; above T_g it is large, below it is much smaller (some authors take it to be zero, but we find in Section 3 that a small finite value may be more realistic). The probability, p_z , is then the chance that, adjacent to a jumping segment, a local free volume of f_c or greater is available (f_c is the fractional volume required to accommodate the jumping segment). This probability (Bueche, 1953) is:

$$p_z = \exp - \left(\frac{Af}{f_v} \right) \quad (12)$$

Then the viscosity at temperature T , relative to that at T_g is given by $\eta(T)/\eta(T_g) = p_z(f)/p_z(f_g)$, or:

$$\frac{\eta(T)}{\eta(T_g)} = \exp \left\{ \frac{Q}{R} \left(\frac{1}{T} - \frac{1}{T_g} \right) \right\} \exp \left(B \left(\frac{1}{f} - \frac{1}{f_g} \right) \right) \quad (13)$$

where $B = Af_c$. Well below T_g the free volume is almost independent of temperature (Fig. 10); then the first term is dominant and we find Arrhenius behaviour (though with a spectrum of activation energies). At and just above T_g , on the other hand, f_v increases rapidly with temperature; and it is probable that Q , correspondingly, decreases: then the second term is dominant. Experiments on viscous liquids support this view: Doolittle (1951, 1952) presents data which are well described by:

$$\frac{\eta(T)}{\eta(T_g)} = \exp \left\{ B \left(\frac{1}{f} - \frac{1}{f_g} \right) \right\} \quad (14)$$

with the constant B close to unity. Substituting eqn. (11) leads immediately to the WLF equation:

$$\log a_T = \log \frac{\eta(T)}{\eta(T_g)} = \frac{- (B/2.3 f_g)(T - T_g)}{f_g/\alpha_f + T - T_g} \quad (15)$$

with $C_1 = - B/2.3 f_g$ and $C_2 = f_g/\alpha_f$. One of the many achievements of the work of Ferry and his co-workers (Williams et al., 1955; Ferry, 1961) is the demonstration that C_1 and C_2 are universal constants at and above T_g . The same constants describe polymers also, implying that f_g and α_f , too, are universal constants. It is helpful to note their magnitudes: taking $B = 1$, the fractional free volume at the glass temperature, f_g , is found to be 0.025; and the free-volume expansion coefficient above T_g , α_f , is $4.8 \times 10^{-4}/K$. Both values are physically plausible. But, as before, the simple rheological model of Fig. 4(a) leads to a modulus which decreases too steeply with temperature. A much better fit to the data is given by the distributions of Fig. 4b, introducing (as before) one new parameter: the standard deviation $\sigma = \Delta C_1/C_1$, and using it in the same way that $\Delta Q/Q_m$ was used earlier.

The Rubbery Modulus

Above T_g , the modulus of linear, amorphous polymers often show a plateau at around 1 MPa. This is close to the modulus of weakly cross-linked rubbers and arises, as far as is known, in a similar way. In the rubbery state, the weak intermolecular (Van der Waals) bonds have

largely melted. The long chain-like molecules can assume a variety of configurations in response to the thermal vibration which causes a "micro-Brownian" motion of the units of the chain. The most probable configurations are those which maximise the entropy of the system. But there is a constraint; the molecular chains curl and twist around each other; in places they form mechanical entanglements which behave very like chemical cross-links (Fig. 11). When strained, the chains tend to order (by lining up) and the entropy decreases; they are prevented from wriggling back to a disordered state by the entanglements. The rubbery modulus is related to this change of entropy by an equation which is the analog, for entropy-induced elasticity, of eqn. (2):

$$E = T \frac{d^2 S(\epsilon)}{d\epsilon^2}$$

where $S(\epsilon)$ is the entropy per unit volume as a function of tensile strain ϵ .

Standard texts (Treloar, 1958; Ward, 1971; Young, 1981) summarise the calculation of the rubbery modulus from this entropy-dominated model. For small strains the result is:

$$E = \frac{3 \rho(T) RT}{\bar{M}_e} \quad (16)$$

where $\rho(T)$ is the density of the rubbery polymer, R is the gas constant, T the temperature and \bar{M}_e is the average molecular weight between cross-links or (here) entanglement points.

The statistical mechanics of entanglements in linear polymers is, at present, beyond the scope of rubber theorists; \bar{M}_e cannot be calculated and is derived instead from data for E by using eqn. (16); values are listed in Table 2. This means that the entropy model of rubber elasticity has not, strictly speaking, been verified for linear polymers, although it is difficult to visualise another cause for the rubbery behaviour; and the values of \bar{M}_e derived from the equation are physically sensible.

At first sight, eqn. (16) suggests that the modulus in the rubbery regime should increase with increasing temperature, and for many cross-linked rubbers, it does. But the density decreases with increasing temperature. If the density at some reference temperature (say, T_g) is $\rho(T_g)$ and the volumetric coefficient of thermal expansion is α_v , then

the density at some higher temperature T is:

$$\rho(T) = \frac{\rho_g}{1 + \alpha_v(T - T_g)} \quad (17)$$

This change in density (which is included in our calculations) cancels, to some extent, the explicit temperature dependence of eqn. (16). Further, it is likely that the weaker entanglements unravel as the temperature is increased so that \bar{M}_e , too, increases with temperature. The combined influence of this and of thermal expansion leads to the plateau (usually with a slight negative slope) seen in experiments.

Rubbery and Newtonian Viscous Flow

At high temperatures ($T \gtrsim 1.2 T_g$) the Van der Waals bonds melt completely and even the entanglement points slip. This is the regime in which thermoplastics are moulded; the polymer behaves like a viscous liquid. For a given polymer system (such as PMMA) the viscosity, η , depends on the molecular weight, \bar{M}_w and the temperature T . The time-and-temperature dependent modulus (at constant stress) is simply:

$$E = \frac{\eta(T)}{t} \quad (18)$$

Two regimes of flow have been identified. Immediately after the rubber plateau, the polymer flows in a way which has the same time-temperature equivalence as that of the visco-elastic regime (eqn. 9) implying that it is controlled by free volume. This is generally called "rubbery flow". Then the viscosity is given by:

$$\eta = \eta_0 \exp - \frac{C_1(T - T_g)}{C_2 + T - T_g} \quad (19)$$

At higher temperatures and low shear rates, flow becomes Netwonian viscous, and follows an Arrhenius law with a narrow spectrum of activation energies, so that:

$$\eta = \eta_0 \exp \frac{Q_m}{RT} \quad (20)$$

The value of η_0 depends on the molecular weight, \bar{M}_w , in one of two ways. Below a critical molecular weight, M_{cr} , the viscosity is proportional to molecular weight so that:

$$\eta = \eta_{cr} \frac{\bar{M}_w}{M_{cr}} \quad (21)$$

where η_{cr} is the viscosity of a melt with molecular weight M_{cr} . But above M_{cr} , the dependence changes such that:

$$\eta = \eta_{cr} \left(\frac{\bar{M}_w}{M_{cr}} \right)^{3.4} \quad (22)$$

Commercial polymeric systems are in this second regime; and in the range of temperatures covered by the diagrams shown in the next section, rubbery flow dominates.

The understanding of this behaviour is still incomplete. Progress in physical modelling has been made by Doi and Edwards (1978a,b,c, 1979) who extended work of Rouse (1953) and of De Gennes (1971) to describe the process of polymer-chain reptation. The polymer chains behave like tangled, flexible strings, each enclosed in a tube made up of the surrounding mass of polymer (Fig. 8). Extension or shear of the polymer requires the diffusive motion of the string in its tube. In the Rouse (1953) approach, the Brownian motion is resisted by a Stokes friction; equivalently, compressive or tensile kinks are formed on the chain and diffuse along its length (Fig. 9): the passage of one kink along the entire chain displaces it by the kink-strength, b . If the chains are short and straight, as in Fig. 9, the time required for a kink to diffuse along a chain is simply proportional to the molecular weight. But if the chains are long and tangled, the (stress-based) random walk, or reptation, of a chain in its tube is more complicated. Doi and Edwards (1978a,b,c,) and Doi (1983) show that the viscosity should then vary as \bar{M}_w^3 , in fair agreement with the observations described by eqn. (22).

Data for the quantities η_0 , \bar{M}_w , M_{cr} are listed in Table 2.

Decomposition

If the polymer gets too hot, the thermal energy exceeds the cohesive energy of some part of the molecular chain causing depolymerisation or degradation. Some (like PMMA) decompose into monomer units; others (PE, for instance) randomly degrade into many products. It is commercially important that no decomposition takes place during high temperature moulding, so a maximum safe working temperature is specified for each polymer; typically, it is about $1.5 T_g$ (Table 2). We have truncated the deformation diagrams at this temperature.

3. DATA FOR PMMA AND PS

In the last section, we discussed constitutive laws for each of the four main deformation regimes. We now fit data to these laws, extracting values of the parameters (like E_0 , α_m , Q_m , ΔQ , T_g , etc.) which best describe the data. The final choice of parameters has already been presented in Table 2. But the method used to obtain them is an important part of the process for constructing the maps shown later. The data are drawn from many sources, referenced in the text and on the figures.

Thermal and Structural Data

Glass temperatures, measured calorimetrically and by dilatometry, are listed in Table 3. We have selected the values shown in Table 2 as the most reliable. The thermal expansion coefficients (Table 2) are from Yannas and Luise (1982), Williams et al. (1965) and Van Krevelen (1976). The molecular weights given in Table 2 are typical values for commercial PMMA and PS, though, in practice, they vary widely depending on the supplier and the grade.

The Glassy Modulus and the Secondary Relaxations

The modulus at absolute zero, E_0 , and its temperature dependence, α_m , were obtained by extrapolation from above 4 K, using the data of

Sinnott (1959, 1962). The values obtained in this way for PMMA are close to the average for all the available data; and those for PS are supported by data from Bondi (1968), (Table 4).

The mean activation energy Q_m for each of the secondary relaxations is found by plotting the log of the time t (or frequency v) for the centre of the transition (or of the damping peak) against $1/T$. It is found (e.g. McCrum, Read and Williams, 1967) that the data follow a simple Arrhenius law:

$$v = \frac{1}{t} \propto \exp - \frac{Q_m}{RT} \quad (23)$$

so that the plot gives a straight line with slope $-Q/2.3R$. For PMMA (Fig. 12a) the β -relaxation has a mean activation of 121 kJ mol^{-1} , in agreement with the measurements of Iwayanagi and Hidemitsu (1953 a,b) and of Sato et al. (1954). The activation energy for the β -relaxation is 13 kJ mol^{-1} . For PS (Fig. 12b) the β -relaxation has a mean activation energy of 132 kJ mol^{-1} . Only two data points (Crissman et al., 1965; Sinnott, 1962) are available for the δ -relaxation in PS so Q_m was calculated from these directly.

When the transitions are well separated (as they are for PS) the drop in modulus ΔE can be measured directly. When this is not so (as for PMMA), ΔE for each transition is adjusted to give the best fit for the overall drop in modulus. Finally the spread of activation energies, $\Delta Q/Q_m$, is chosen by trial and error to match the breadth of the transition. The parameters which fit various groups of data are listed in Table 5 and abstracted in Table 2. The predictions of the rheological model, using these parameters, are compared with raw data in Figs. 13 (a), (b) and (c). In practice, the δ -transition in PMMA and the γ -transition in PS have a very small effect on the moduli ($\Delta E < 0.1 \text{ GPa}$) and they are ignored in constructing the diagrams.

The Glass-Rubber Transition and the Rubbery Modulus

The glass-rubber transition, too, is modelled by the rheological model shown in Fig. 4(b). The modulus drop ΔE is the difference between the glassy modulus (reduced by the modulus drops associated with the secondary transitions) and the rubbery modulus. The mean value of C_1 and its standard deviation were chosen as described earlier. For PMMA, a standard deviation of 0.055 gives a good fit to data (Fig. 14a); for PS, the value 0.08 gives a good fit (Fig. 14b).

The rubbery modulus is related to the molecular weight between entanglements \bar{M}_e , by eqn. (16). The most recent measurements for commercial polymers are those of Seitz (1979) and it is his data that we have used to select \bar{M}_e for PS. But for PMMA a range of values for the rubbery modulus and density have been reported. Results derived from these are listed in Table 6; the value we have selected for M_e is about half the value given by Seitz. The density $\rho(T_g)$ at the glass temperature was calculated by extrapolating data for ρ from the measurement temperature to T_g .

Figure 15 shows the experimental shift factors, $\log a_T$, for PMMA and PS. Above T_g they are well fitted by the WLF equation (eqn. 9) with values of C_1 and C_2 which are consistent with values of f_g and a_f listed in Table 7. The figures show that at T_g there is a discontinuity in slope of the shift factor. The expansion data given in Table 7 suggest that a_f is smaller below T_g , but that it is not zero. We have therefore used the WLF equation below T_g , with a new value of C_2 , calculated from the data in Table 7. The final choice of C_1 and C_2 are listed in Table 2. The viscosity in the viscoelastic transition has been calculated as described in Section 2, using these parameters in the WLF equation.

Rubber (Glass) - Viscous Transition and Decomposition

Data for viscous flow are summarised in Table 8. The modulus is calculated by using eqn. (19) with the data listed in Table 2, including a spread of the constant C_1 . Decomposition data are summarised in Table 9.

4. DEFORMATION-MECHANISM DIAGRAMS

Construction and Features of the Diagrams

The previous sections have described the broad regimes of deformation behaviour for linear amorphous polymers, between absolute zero and the decomposition temperature. Physical models exist for each deformation mode, leading to constitutive laws which describe the time and temperature dependent modulus E ; the values of the parameters which enter the laws are known, at least approximately (Table 2).

We now ask: over what range of time and temperature is a given mechanism dominant? And when do the changes of mechanism appear? For each mechanism, the constitutive equation takes the form:

$$E = f(t, T, \text{material parameters})$$

(or

(24)

$$E = f(v, T, \text{material parameters})$$

where t is the loading time (or v is the frequency) and T is the absolute temperature. The dominant mechanism for a given T and t is the one which leads to the lowest value of E . Mechanism changes take place along the lines obtained by equating pairs of the constitutive laws.*

Figures 16 to 19 show deformation mechanism diagrams for PMMA and PS, constructed from the constitutive laws of Section 2, using the parameters of Table 2, combined in the way we have just described, and detailed in the Appendix. They show the time- and temperature-dependent modulus, E , for a number of different loading conditions, as a function of temperature and frequency of loading.

Figures 16 and 17 show the dynamic modulus of PMMA over the full ranges of temperature and frequency that can be realised in practice. In Fig. 16,

*The response of the rheological model for the relaxations is evaluated numerically, summing the Gaussian distribution of activation energies over $3\Delta Q$ on either side of Q .

the axes are E and T ; the contours are lines of constant frequency. The four regions are roughly distinguished by the range of modulus which characterises them, as suggested by Tobolsky (1960), though strictly it is a field of values of E , T and ν , not merely of E , which characterises a mechanism. In Fig. 17 the axes are E and ν (plotted inversely to make the diagram comparable with diagrams which have time as abscissa: see Gilbert, 1984). Here, too, the four mechanism-regimes are distinguished by a range of values of E . Figures 18 and 19 show similar diagrams for PS. They closely resemble those for PMMA.

Influence of Polymer Chemistry and Molecular Weight

It seems probable that these diagrams for PMMA and PS are broadly typical of those for linear amorphous polymers. By normalising the temperature scale by T_g , the lowest-order effect of differing polymer chemistry are removed.

At any more detailed level, of course, there are effects of polymer chemistry and molecular weight. In the glassy regime the secondary transitions are determined by the nature of the side-groups, since these influence the packing of molecules in the amorphous state and so define the width of the transitions. (The experiments of Fujimo et al. (1961), on co-polymers of PMA and PMMA, for example, show that the larger the sidegroups, the more difficult it is to pack the chains, and the broader is the glass-rubber transition.) The extent of the rubbery regime, too, depends on the molecular weight of the polymer. Reducing the molecular weight shifts the contours in the viscous flow regimes to the left, and reduces the extent of the rubbery plateau or removes it altogether. McLoughlin and Tobolsky (1952), for instance, find that PMMA with a molecular weight of 3600 kg/mol shows a pronounced rubbery plateau, while that with a molecular weight of 150 kg/mol shows none. Other studies of the extent of the rubbery regime can be understood in these terms (Vinogradov et al., 1971). And the viscosity of the melt regime, too, depends on molecular weight (Van Krevelin, 1976), though the differences scale, broadly, as T_g .

We expect, therefore, that linear amorphous will be described by diagrams like those of Figs. 16 to 19, with small differences caused by molecular weight and architecture.

5. SUMMARY AND CONCLUSIONS

GAB3, Disc 8

Maps can be constructed which summarise the time-and-temperature dependent modulus of amorphous polymers, $E(t,T)$, for a wide range of temperatures and times, under various loading conditions. Several separate mechanisms are involved: bond stretching, constrained molecular movement and larger scale molecular sliding, rubbery behaviour constrained by entanglements and true viscous flow. Each mechanism can be modelled (though with differing levels of physical realism) to give constitutive equations which describe how the modulus $E(t,T)$ depends on temperature, time or frequency of loading, and on material parameters which characterise the chemistry and molecular architecture of the polymer. We have assembled material parameters for PMMA and for PS and used them, with the constitutive equations, to construct the maps shown as Figs. 16 to 19.

It is probable that the maps shown here are broadly typical of linear amorphous polymers (though maps for others can readily be constructed using the same method). The same approach can be adapted to describe amorphous thermosets and rubbers, and, with further changes, to commercially significant semicrystalline polymers such as Nylon and PE.

The maps shown here describe small-strain behaviour. The next step, we believe, is to develop a parallel approach for large strain deformation which is capable of including cold drawing, shear banding, twinning and crazing.

ACKNOWLEDGEMENTS

We wish to thank Dr. L.M. Brown, Dr. D.J. Brown, Mr. P.A. Smith and Dr. A.M. Donald for many very helpful discussions. We wish to acknowledge the support of the U.S. Army European Research Office through a research contract, and the S.E.R.C. through the award of a studentship.

REFERENCES

GAB4, Disc 8

- Arridge, R.F.C. (1975) "Mechanics of Polymers", Oxford University Press, Oxford.
- Berry, G.C. and T.G. Fox (1967) Adv. Poly. Sci. 5, 261.
- Bondi, A. (1968) "Physical Properties of Molecules, Crystals, Liquids and Glasses", Wiley, New York, 394.
- Bowden, P.B. (1968) Polymer 9, 449.
- Brady, T.E. and G.S.Y. Yeh (1971) J. Appl. Phys. 42, 4622.
- Brown, L.M. (1982) Proc. 3rd Riso Conference, E. Lilholt and R. Talreja, Riso National Lab., Denmark, p.1.
- Bueche, F. (1953) J. Chem. Phys. 22, 603.
- Cohen, M.H. and D. Turnbull (1959) J. Chem. Phys. 31, 1164.
- Connor, T.M. (1970) J. Poly. Sci. A2, 191.
- Crissman, J.M., A.E. Woodward and J.A. Sauer (1964) J. Poly. Sci. A3, 5075.
- Crissman, J.M., A.E. Woodward and J.A. Sauer (1965) J. Poly. Sci. A2, 2693.
- De Gennes, P.G. (1971) J. Chem. Phys. 55, 572.
- Deutsch, K., E.A.W. Hoff and W. Reddish (1954) J. Poly. Sci. 13, 565.
- Doi, M. (1983) J. Poly. Sci. Poly. Phys. 21, 667.
- Doi, M. and S.F. Edwards (1978) J. Chem. Soc., Faraday Trans. 2 74, 1789.
- Doi, M. and S.F. Edwards (1978) J. Chem. Soc., Faraday Trans. 2 74, 1802.
- Doi, M. and S.F. Edwards (1978) J. Chem. Soc., Faraday Trans. 2 75, 38.
- Doi, M. and S.F. Edwards (1979) J. Chem. Soc., Faraday Trans. 2 74, 1818.
- Doolittle, A.K. (1951) J. Appl. Phys. 22, 1471.
- Doolittle, A.K. (1952) J. Appl. Phys. 23, 236.
- Dosser, J.M. (1983) ICI Petrochemicals and Plastics (Private communication).
- Ferry, J.D. (1961) "Viscoelastic Properties of Polymers", Wiley, N.Y., Ch. 11.
- Fox, T.G. and P.J. Flory (1950) J. Appl. Phys. 21, 581.
- Fox, T.G., S. Gratch and S. Loshaek (1956) "Rheology: Theory and Applications", F.R. Eirich, Ed. Academic Press, New York 1, Chapt. 12.
- Fox, T.G. et al. (1958) J. Am. Chem. Soc. 80, 1768.

- Flory, P.J. (1969) "Statistical Mechanics of Chain Molecules", Interscience, New York.
- Frost, H.J. and M.F. Ashby (1982) "Deformation Mechanism Maps", Pergamon Press, Oxford.
- Fujino, K. et al. (1961) J. Colloid Sci. 16, 262.
- Fujino, K., K. Senshu and H. Kawai (1962) Rept. Prog. Poly. Phys. (Japan) 5, 107.
- Gall, W.G. and N.G. McCrum (1961) J. Poly. Sci. 50, 489.
- Gilbert, D.G. (1984) Ph.D. Thesis, Engineering Dept., Cambridge University.
- Graessley, W.W. (1982) Ad. Poly. Sci. 47, 67.
- Haward, R.N. (1973) in "The Physics of Glassy Solids" Ed. R.N. Haward, Appl. Sci. London p.1.
- Heijboer, J. (1956) Kollid-Z. 148, 36.
- Heijboer, J. (1965) "Physics of Non-Crystalline Solids", North Holland, Amsterdam, 231.
- Hendus, H. et a. (1959) Ergeb. Exakt. Naturw. 31, 220.
- ICI Technical Service Note (1981), "Diakon", DN23, 4th edition.
- Illers, K.M. and E. Jenckel (1958) Rheol. Acta. 1, 322.
- Illers, K.M. and E. Jenckel (1959) J. Poly. Sci. 41, 528.
- Iwayanagi, S. and T. Hidehsima (1953a) J. Phys. Soc. (Japan) 8, 365.
- Iwayanagi, S. and T. Hidemitsu (1953b) J. Phys. Soc. (Japan) 8, 368.
- Johnson, F.A. and J.C. Radon (1972) Eng. Fract. Mech. 4, 555.
- Kolb, M.J. and E.F. Izard (1949) J. Appl. Phys. 20, 564.
- Krevelen, Van D.W. (1976) "Properties of Polymers", Elsevier, Amsterdam.
- Loshaek, S. (1955) J. Poly. Sci. 15, 391.
- Masuda, T., K. Kitagawa and S. Onogi (1970) Poly. J. (Japan) 1, 418.
- McCrumb, N.G. and E.L. Morris (1964) Proc. Roy. Soc. A281, 258.
- McCrumb, N.G., Read, B.E. and Williams, G. (1967) "Anelastic and Dielectric Effects in Polymer Solids", Wiley, London.
- McLoughlin, J.R. and A.V. Tobolsky (1952) J. Colloid. Sci. 7, 555.
- Natta, G. (1955) J. Poly. Sci. 16, 143.
- Onogi, S., T. Masuda and K. Kitagawa (1970) Macromol. 3, 109.

Powles and Mansfield (1962).

Plazek, D.J. (1965) J. Phys. Chem. 69, 3480.

Rogers, S.S. and L. Mandelkern (1957) J. Phys. Chem 61, 945.

Rouse, Jr., P.E. (1953) J. Chem. Phys. 21, 1272.

Sato, K. et al. (1954) J. Phys. Soc. (Japan) 9, 413.

Schmeider, von K. and K. Wolf (1953) Kolloid-Z. 134, 149.

Seitz, J.T. (1979) 50th Golden Jubilee of the Rheology Soc., Boston, Mass.

Shell Plastics (1983) Technical Bulletin PS2.1 "Shell Polystyrene Safety Data and Information".

Sinnott, K.M. (1959) J. Poly. Sci. 35, 272.

Sinnott, K.M. (1960) J. Poly. Sci. 42, 3.

Sinnott, K.M. (1962) Soc. Plastic. Engrs. Trans. 2, 63.

Tobolsky, A.V. (1960) "Properties and Structure of Polymers", Wiley, New York.

Treloar, L.R.G. (1958) "The Physics of Rubber Elasticity", Clarendon Press, Oxford.

Vinogradov, G.V. et al. (1971) J. Poly. Sci. A2, 1153.

Williams, M.L., R.L. Landel and J.D. Ferry (1955) J. Am. Chem. Soc. 77, 3701.

Ward, I.M. (1971) "Mechanical Properties of Polymers", Wiley, New York.

Yannas, I.V. (1974) "Deformation in Glassy Polymers - Molecular Interpretation", Proc. IUPAC Symp., Rio de Janeiro, Elsevier, Amsterdam.

Yannas, I.V. and R.R. Luise (1982) J. Macromol. Sci. Phys. B21, 443.

Yannas, I.V. and A.C. Lunn (1971) Polymer Lett. 9, 611.

Yano, O. and Y. Wada (1971) J. Poly. Sci. A2, 669.

Young, R.J. (1981) "Introduction to Polymers", Chapman and Hall, London.

Williams, J.T. and K.J. Cleereman (1952) "Styrene, Its Polymers, Co-polymers and Derivatives", Boundy, R.H. and R.F. Boyer, Eds. Reinhold Pub. Corp. New York 2, Chapt. 10.

Wittmann, J.C. and A.J. Kovacs (1969) J. Poly. Sci. C16, 4443.

TABLE 3: GLASS TRANSITION TEMPERATURES (HIGH M_w)

Material	Glass Temperature, T_g (K)
PMMA	378 ^{a)} , 378 ^{b)} , 377 ^{c)} , 377 ^{d)} , 388 ^{e)} , 378 ^{f)} , 378 ^{g)}
PS	373 ^{h)} , 373 ⁱ⁾ , 389 ^{j)} , 373 ^{g)} ,

a) Loshaek (1955); b) Rogers and Mandelkern (1957); c) Wittmann and Kovacs (1969); (d) Fox et al. (1958); e) Berry and Fox (1967); f) Van Krevelen (1976); g) Fox et al. (1976); h) Fox and Flory (1950); i) Plazek (1965); (j) Schmeider and Wolf (1953).

TABLE 4: YOUNG'S MODULUS AND TEMPERATURE DEPENDENCE*

Polymer	Modulus, E_0 GPa	α_m
PMMA	8.57 ^{a)}	0.28 ^(a)
	10.51 ^{b)}	-
	7.70 ^{c)}	-
PS	6.21 ^{d)}	0.28 ^{d)}
	5.80 ^{b)}	
	6.25 ^{c)}	

* E_0 is Young's Modulus extrapolated to 0 K; α_m is the normalised temperature dependence (eqn. 3).

- a) Sinnott (1959) Extrapolated from 4 K and calculated from G assuming $v = 0.33$.
- b) Yannas and Luise (1982) Numerical average from other sources (c) and (d) are included in the PS average.
- c) Bondi (1968).
- d) Sinnott (1962) Extrapolated from 4 K and calculated from G assuming $v = 0.33$.

TABLE 5: SECONDARY TRANSITION DATA

Polymer	Transition	Q_m (kJmol ⁻¹)	T* (K)	ΔE (GPA)	ΔQ (kJmol ⁻¹)
PMMA	β	75.4 ^{a)} 121.5 ^{b)} 75.4 ^{c)} 125.7 ^{d)} 71.2 ^{e)}	283 ^{l)}	3.55 ^{p)}	24 ^{p)}
PMMA	γ	13.0 ^{f)}	100 ^{m)}	1.66 ^{p)}	2.57 ^{x)}
PMMA	δ	<20.9 ^{g)}	<4.2 ⁿ⁾	<0.1 ⁿ⁾ <0.1 ^{q)}	-
PS	β	125.7 ^{h)} 138.3 ⁱ⁾	300 ^{o)}	0.2 ^{p)}	55 ^{x)}
PS	γ	33.5 ^{j)}	132 ^{j)}	<0.07 ^{r)} 0.075 ^{j)}	-
PS	δ	9.4 ^{k)}	36 ^{k)}	1.79 ^{s)} 0.9 ^{t)} >1. ^{u)} >0.5 ^{w)}	5 ^{x)}

* Q_m is the mean activation energy, T* the temperature characterising the damping peak at a frequency of 1 Hz, ΔE the modulus drop associated with the transition and ΔQ the spread in Q required to fit the experimental data.

- a) Deutsch et al 1954
- b) Iwayanagi and Hidemitsu 1953a, 1953b
- c) Heijboer 1956
- d) Sato et al 1954
- e) McCrum and Morris 1964
- f) Sinnott 1960
- g) Johnson and Radon 1972
- h) Yano and Wada 1971
- i) Connor 1970
- j) Illers and Jenckel 1959
- k) Calculated from s) and t)
- l) Illers and Jenckel 1959
- m) Calculated from s) and t)
- n) Heijboer 1965
- o) Powles and Mansfield 1962
- p) Sinnott 1959
- q) Illers and Jenckel 1958
- r) Best fit to data this study
- s) Crissman et al 1964, 1965
- t) Schmieder and Wolf 1953
- u) Crissman et al 1965
- v) Sinnott 1962
- w) Bondi 1968
- x) Hendus et al 1959
- y) Estimated value using the method described in the text

TABLE 6: MOLECULAR ENTANGLEMENT WEIGHT, DENSITY AND EXPANSION COEFFICIENTS

Polymer	\bar{M}_e (kg/mol)	ρ (10^3 kg/m 3)	α_g (K $^{-1}$)	α_v (K $^{-1}$)	$\rho(T_g)$ (10^3 kg/m 3)
PMMA	9.15 ^{a)}	1.188 ^{d)}	2.7×10^{-4} ¹⁾	6.2×10^{-4} ¹⁾	1.16 ^{m)}
	10.0 ^{b)}	1.195 ^{e)}			
		1.188 ^{f)}			
		1.150 ^{g)}			
		1.216 ^{h)}			
		1.19 ⁱ⁾			
PS	19.1 ^{a)}	1.04-1.065 ^{j)}	$1.8^{1)}$ $2.8^{1)}$	$4.5^{1)}$ $7.1^{1)}$	1.03 ^{m)}
	18.1 ^{c)}	1.05 ^{h)}			
		1.057 ^{e)}			
		1.052-1.065 ^{k)}			

* \bar{M}_e is the molecular weight between entanglements, calculated from eqn. (16), ρ is the density at the temperature listed in the reference, α_g is the bulk expansion coefficient below T_g and α_v is that above T_g ; $\rho(T_g)$ is the mean density extrapolated to T_g .

- a) Seitz (1979)
- b) Masuda et al (1970)
- c) Onogi et al (1970)
- d) Fox et al (1958)
- e) Kolb and Izard (1949) at 273 K
- f) Gall and McCrum (1961) at 298 K
- g) Rogers and Mandelkern (1957) at T_g
- h) Fujino et al (1962) at 298 K
- i) Brady and Yeh (1971)
- j) Natta (1955)
- k) Williams and Cleereman (1952)
- l) van Krevelen (1976)
- m) Calculated from data presented

TABLE 7: FREE VOLUME DATA*

Material	α_v at T_g (K ⁻¹)	α_v at T_g (K ⁻¹)	α_o at T_g (K ⁻¹)	α_f ($T < T_g$)	α_f ($T > T_g$)
PMMA	6.25 \times 10 ⁻⁴ , a)	2.69 \times 10 ⁻⁴ , b)	9.4 \times 10 ⁻⁴ , c)	1.75 \times 10 ⁻⁴ , c)	5.31 \times 10 ⁻⁴ , d)
PS	6.12 \times 10 ⁻⁴ , a)	2.27 \times 10 ⁻⁴ , b)	6.8 \times 10 ⁻⁴ , c)	1.69 \times 10 ⁻⁴ , c)	5.4 \times 10 ⁻⁴ , d)

* α_v and α_o are the bulk expansion coefficient above and below T_g . α_o is the expansion coefficient for the occupied volume (Fig. 9). α_f is the difference. C_1 and C_2 in Table 2 are calculated from these data using $C_1 = B/2.303 f_g$ and $C_2 = f_g/d_f$, with $B = 1$ (Williams et al., 1955) and $f_g = 0.025$ (Doolittle, 1951, 1952).

- a) Van Krevelen (1976, Table 4.10)
- b) Average values in ref (a)
- c) Calculated by Gilbert (1984)

TABLE 8: VISCOUS FLOW*

Polymer	η_o N s m ⁻²
PMMA	2 \times 10 ⁻² , a)
PS	1.4 \times 10 ⁻³ , b)

* η_o is the preexponential viscosity in eqn. (19)

- a) Chosen to fit the data of Fujimo et al (1961)
- b) Chosen to fit the data of Fujita and Nimonoya (1957)

TABLE 9: DEPOLYMERISATION TEMPERATURES

Polymer	T_d	T_d/T_g
PMMA	543 ^{a)}	1.44
PS	543 ^{b)}	1.46

a) Dosser 1983

b) Shell Plastics 1983

APPENDIX: COMPUTATION OF THE DEFORMATION DIAGRAMS

GABApp, Disc 8

The modulus E is calculated as a function of temperature T and loading frequency ω ("dynamic loading") as described below. Calculations for modulus as a function of temperature and time ("stress relaxation") follow the same method. The text describes models for the mechanisms of deformation which determine the modulus, E . At the highest temperatures, E is determined by viscous flow. The modulus E_{vR} is then determined by the faster of the two flow mechanisms (eqns. 19 and 20). As the temperature is decreased, E_{vR} increases until it exceeds the rubbery modulus E_R (eqn. 16); then this, not viscous flow, determines the modulus: E is set equal to the lesser of E_{vR} and E_R . Further decrease in temperature introduces the glass-rubber transition. Let the increase in modulus associated with this transition be ΔE_α (defined below). Further drop in temperature freezes out the β , γ and δ relaxations; let the increase in modulus caused by these be E_β , ΔE_γ and ΔE_δ . Then the modulus, at temperature T and frequency ω is:

$$E(T, \omega) = \text{Least of } (E_R \text{ and } E_{vR}) + \Delta E_\alpha + \Delta E_\beta + \Delta E_\gamma + \Delta E_\delta \quad (\text{A1})$$

To proceed further, we require expressions for the individual terms. Consider the δ relaxation as an example. It is described by the array of n Maxwell elements shown in Fig. 4(b). For a single element:

$$\dot{\epsilon} = \frac{\dot{\sigma}}{E} + \frac{\sigma}{\eta}$$

Then for the parallel array of Fig. 4(b), the following constitutive equations hold.

For constant strain:

$$E(T, t) = \sum_{i=1}^n \delta E_i \exp\left(-\frac{\delta E_i t}{\delta \eta_i}\right) \quad (\text{A2})$$

for constant strain rate:

$$E(T, t) = \sum_{i=1}^n \frac{\delta \eta_i}{\tau} \left(1 - \exp\left(-\frac{\delta E_i t}{\delta \eta_i}\right)\right) \quad (\text{A3})$$

and for dynamic loading (so that $\epsilon = \epsilon_0 \sin \omega t$):

$$E(T, w) = \sum_{i=1}^n \left(\frac{\delta E_i}{1 + (\frac{w \delta n_i}{\delta E_i})^2} \right) \quad (A4)$$

This last equation is the one we require for the present problem. Let the total modulus change during the δ transition be ΔE_δ^0 . Then, for this transition:

$$E = \sum_{i=1}^n \left(\frac{\delta E_i}{1 + (\frac{w \delta n_i}{\delta E_i})^2} \right)$$

where $\delta E_i = \Delta E_\delta^0 f(Q) \delta Q$

and $\delta n_i = n_0 \exp \left(\frac{Q_i}{RT} \right) f(Q) \delta Q$.

Similar expressions are used for the β and γ transitions; the glass transition only differs in the expression used for n : it is (eqn. 15):

$$n = n_0 \exp \left(- \frac{C_1 (T - T_g)}{C_2 + T - T_g} \right)$$

The rubbery flow regime is treated in a similar way.

An important quantity in each summation is the standard deviation of the activation energy. It determines, through eqn. (5), the breadth of each transition. The standard deviation of Q (for the β , γ and δ transitions) and of C_1 (for the α and rubbery flow regimes) is listed in Table 2 as the "fractional spread" in each quantity: $\Delta Q/Q_m$ and $\Delta C_1/C_1$.

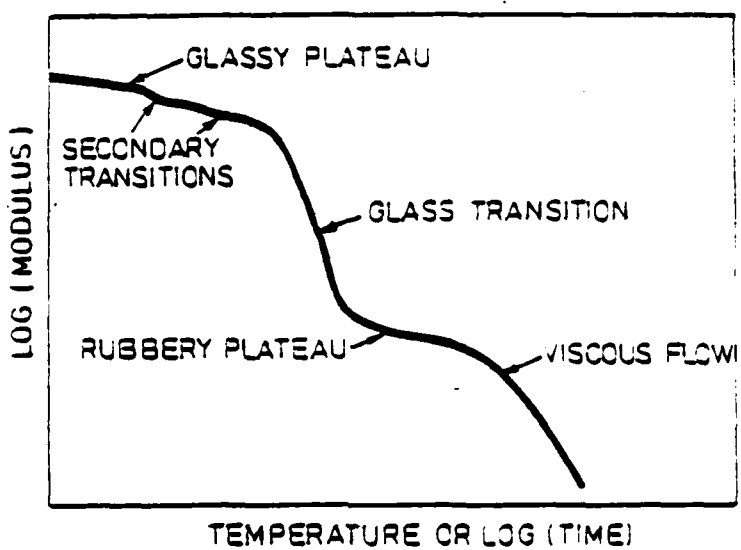


Fig. 1. Schematic showing the regimes of behaviour typical of an amorphous polymer.

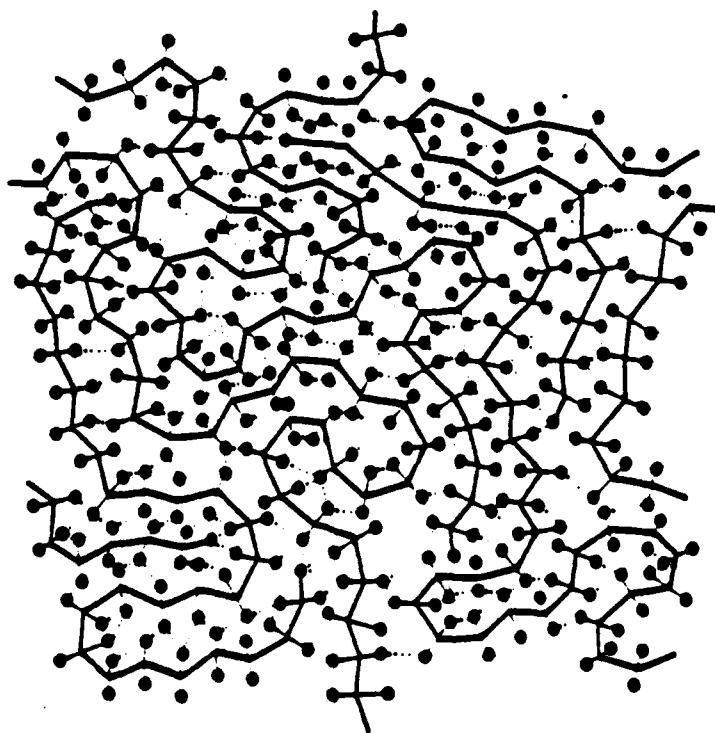


Fig. 2. Schematic of a linear amorphous polymer. The covalently-linked chains (full lines) are bonded to each other by weak Van der Waals forces (dotted lines) which determine the glassy modulus.

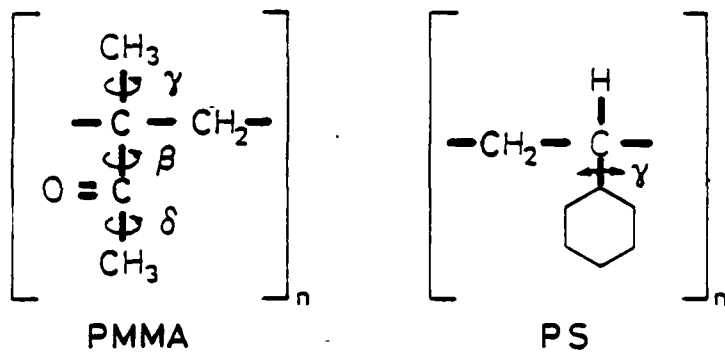


Fig. 3. Schematic of the secondary relaxations in PMMA and PS.

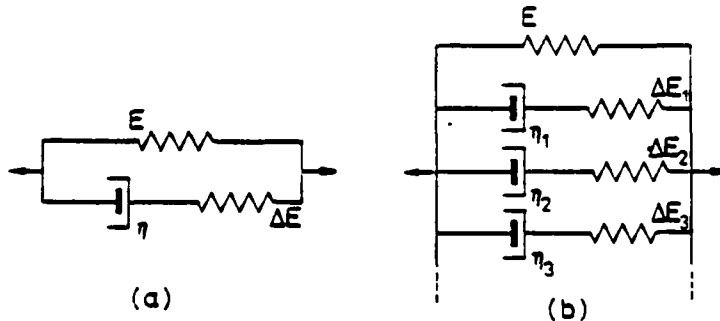


Fig. 4. (a) The standard linear solid; (b) the extended model. If a Gaussian distribution of relaxation times is assumed, the model requires only one more parameter than the standard-linear solid to describe it completely.

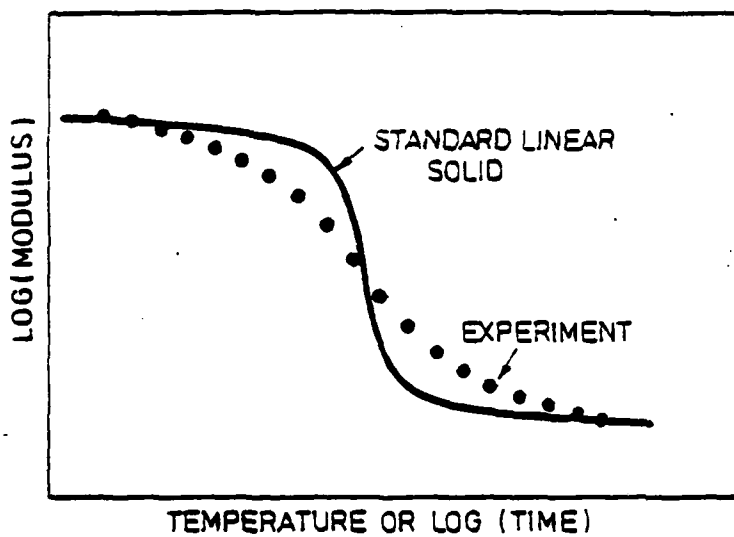


Fig. 5. The response of the standard-linear solid with a single activation energy compared with experiment.

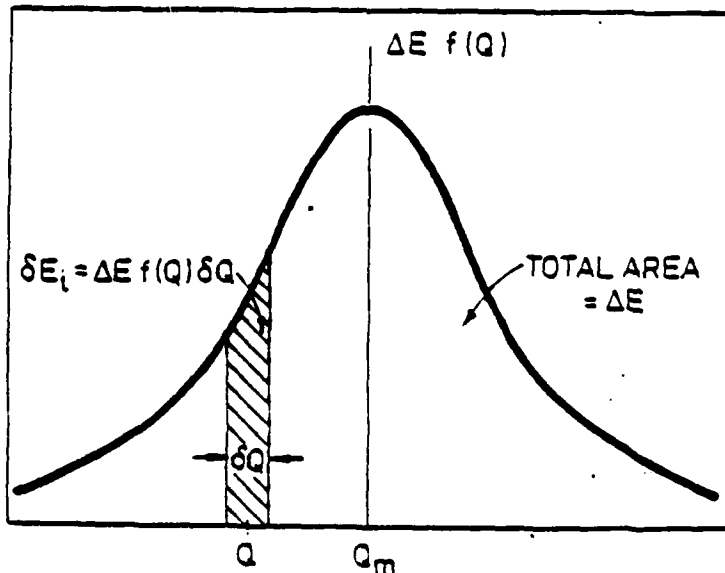


Fig. 6. A Gaussian distribution for the fraction of units with activation energies between Q and $Q + \delta Q$ requires an associated distribution of moduli δE_i , illustrated here.

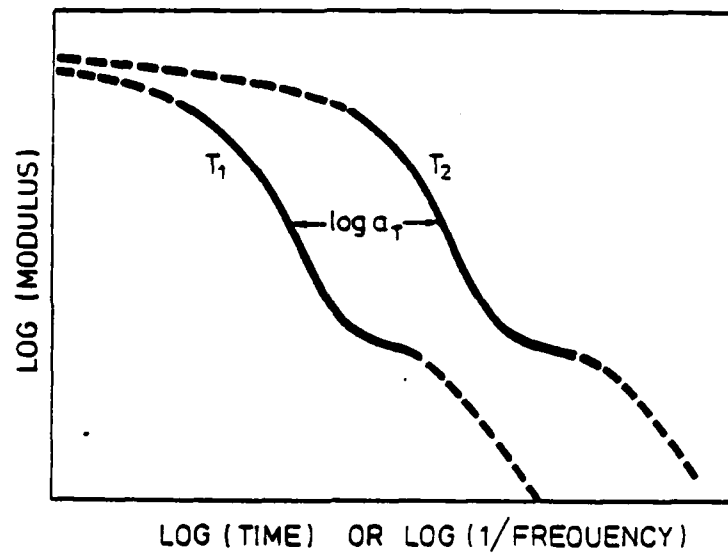


Fig. 7. Schematic of the time-temperature equivalence for the modulus.

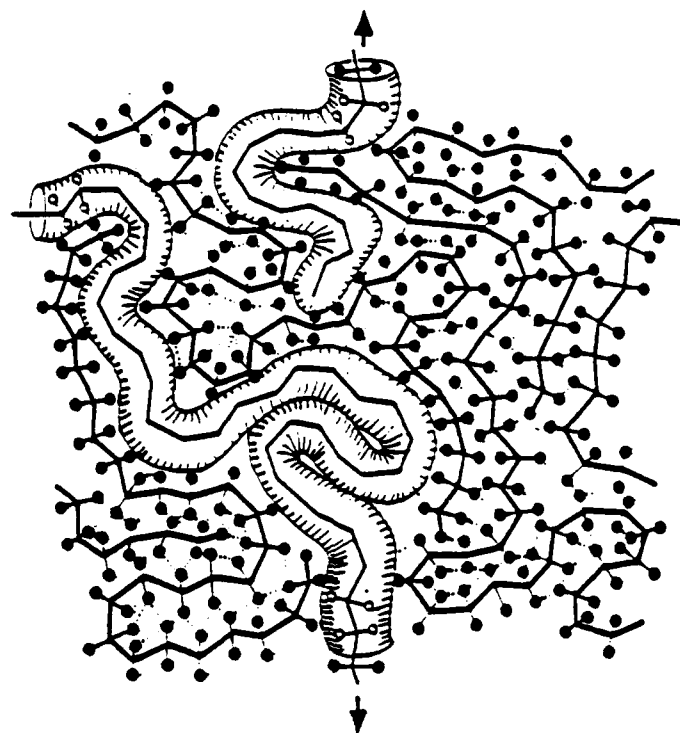


Fig. 8. Schematic of viscous diffusive motion, or reptation, of a polymer chain in the tube defined by its immediate surroundings.

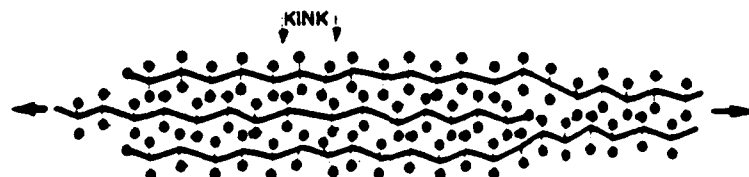


Fig. 9. The diffusion of compressive kinks along a polymer chain, leading to relative motion of chains.

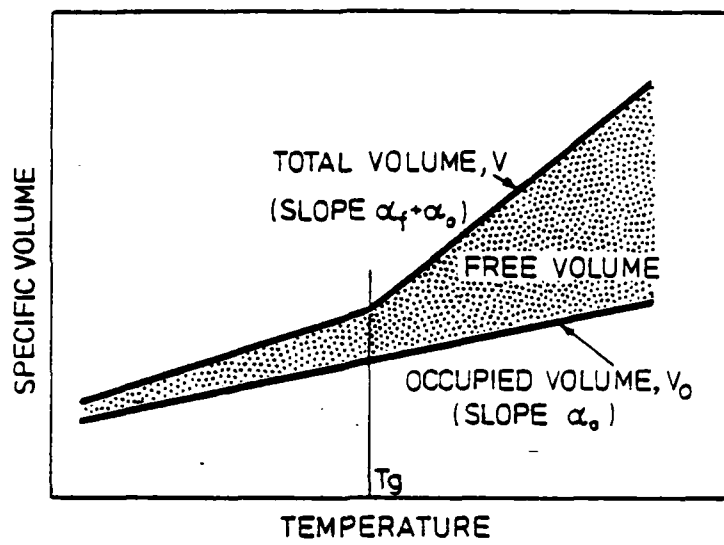


Fig. 10. Typical variation of specific volume with temperature for an amorphous polymer.

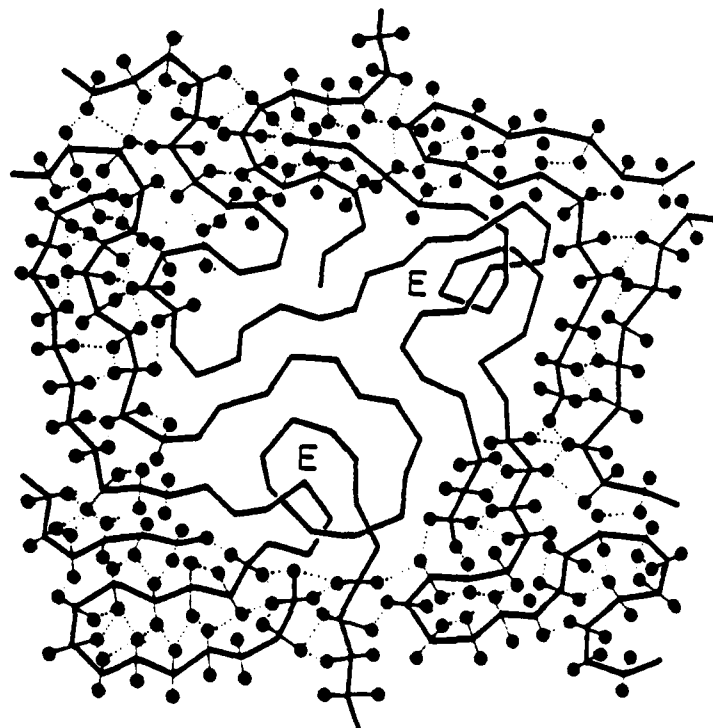


Fig. 11. Schematic of a polymer network showing entanglement points (marked 'E') which act like chemical cross-links.

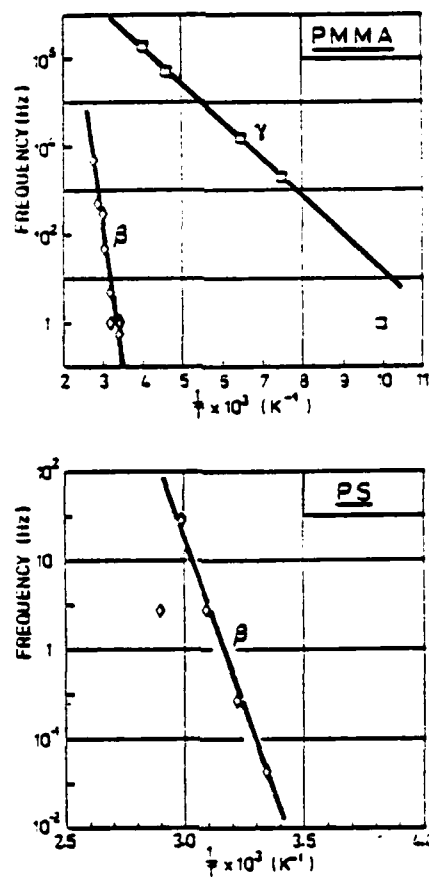


Fig. 12. Arrhenius plots of the frequency of damping peak (a) the β and γ peaks in PMMA; (b) the β peak in PS (after McCrum, Read and Williams, 1967).

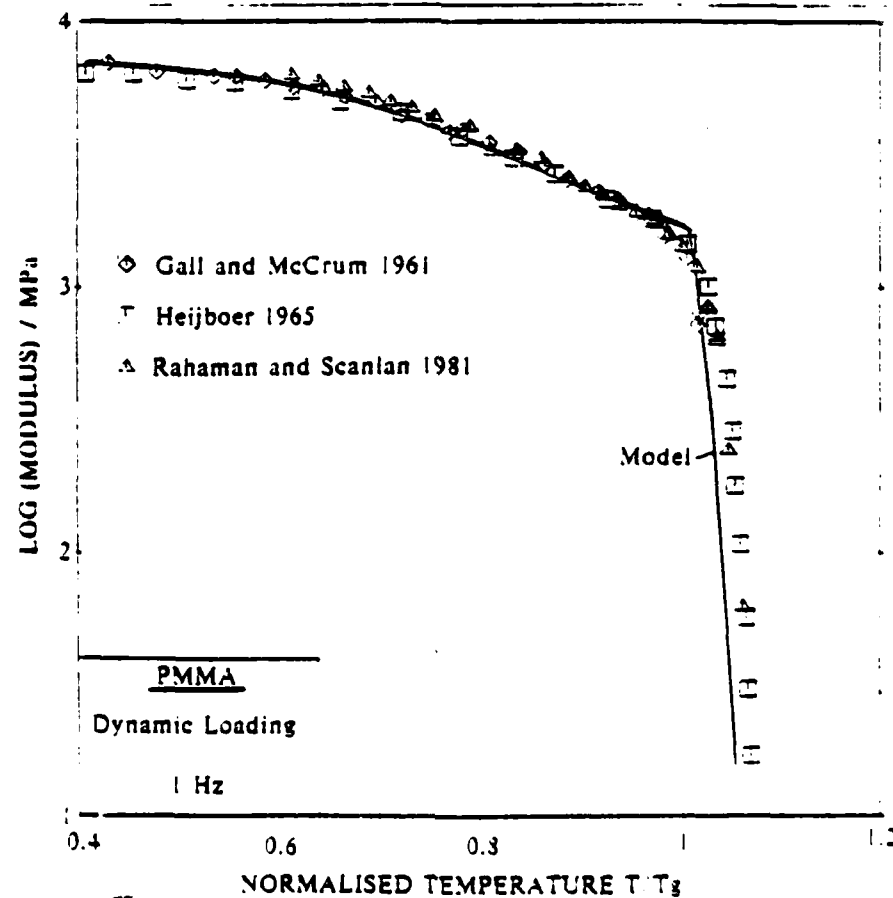


Fig. 13. Comparison of data from various sources with the model:
(a) PMMA at 1 Hz through T

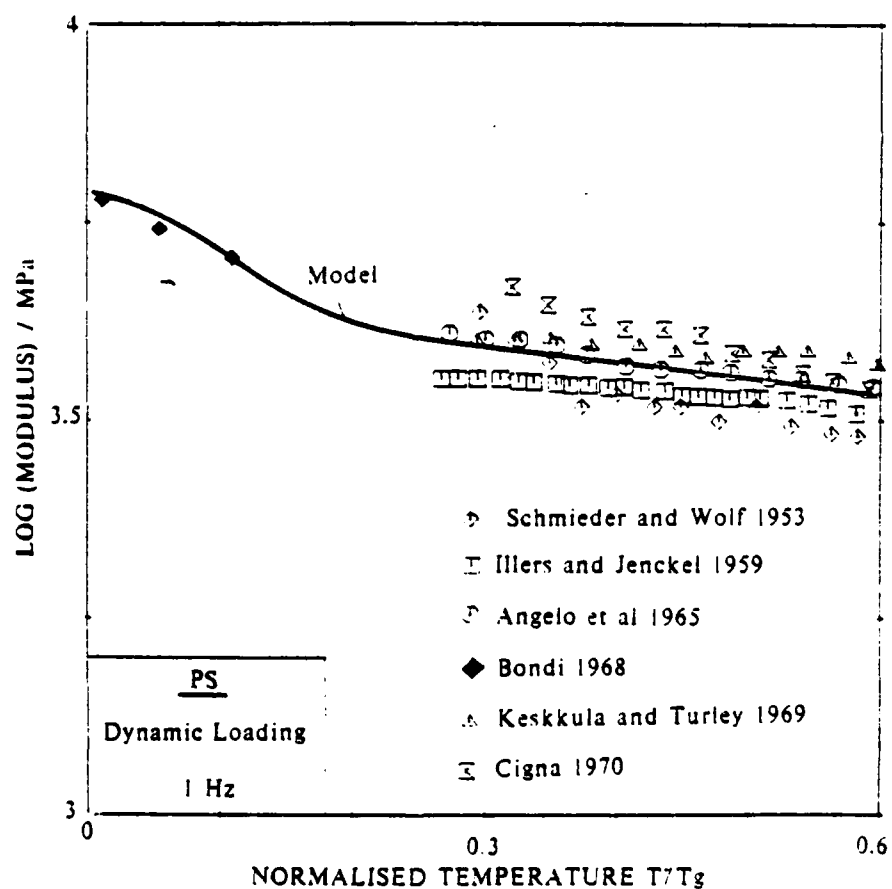
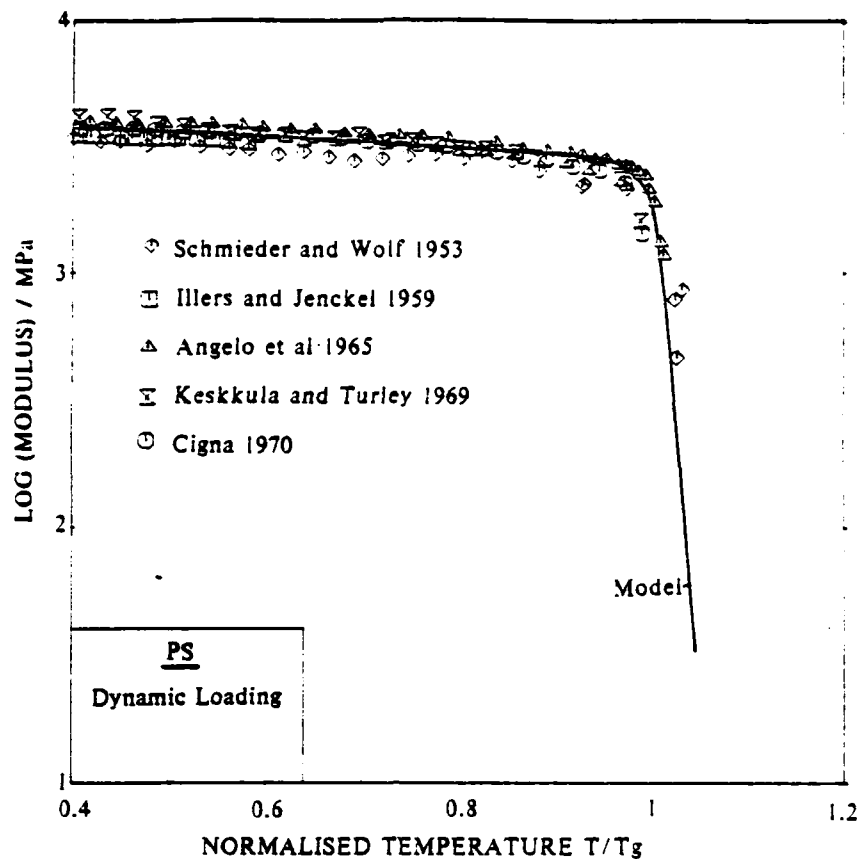


Fig. 13. Comparison of data from various sources with the model:
 (b) PS at 1 Hz through T_g ;
 (c) PS at 1 Hz at low temperature.

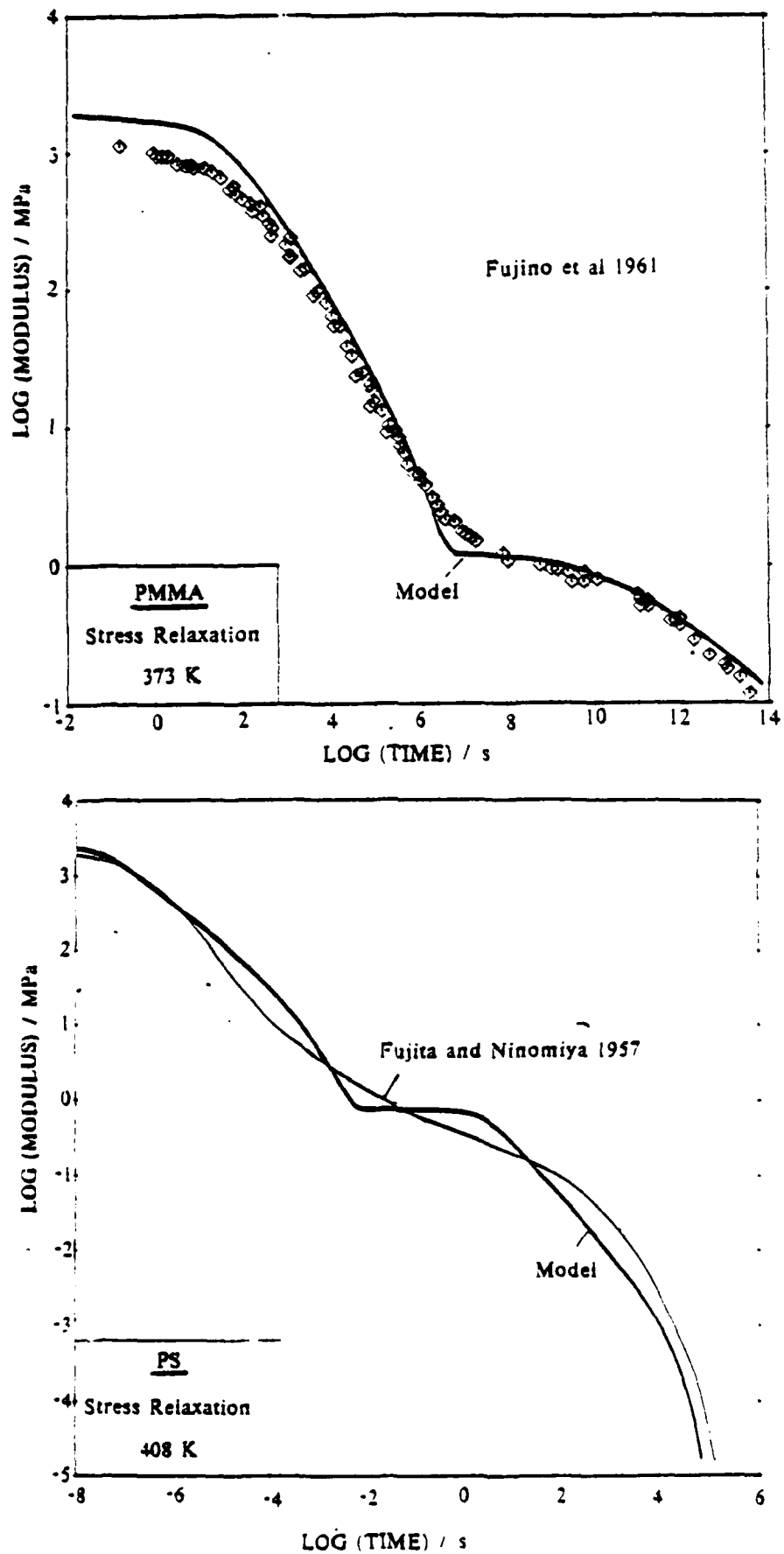


Fig. 11. Comparison of stress relaxation data and the small predictions of the combined models (a) for PMMA at 373 K, and (b) for PS at 408 K.

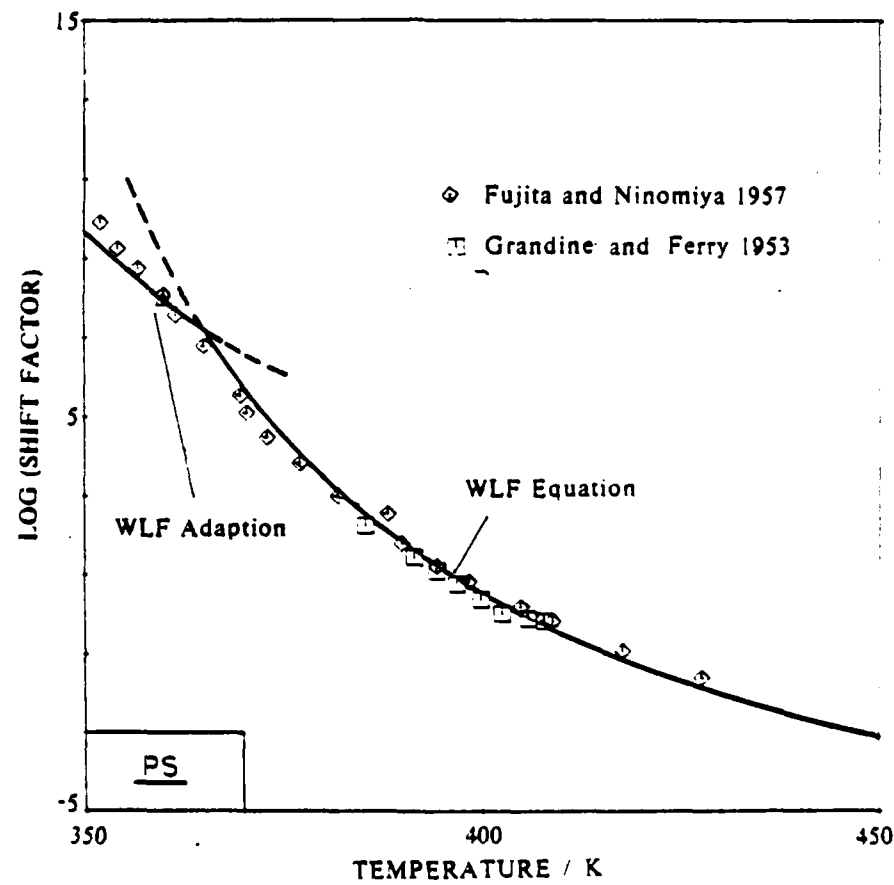
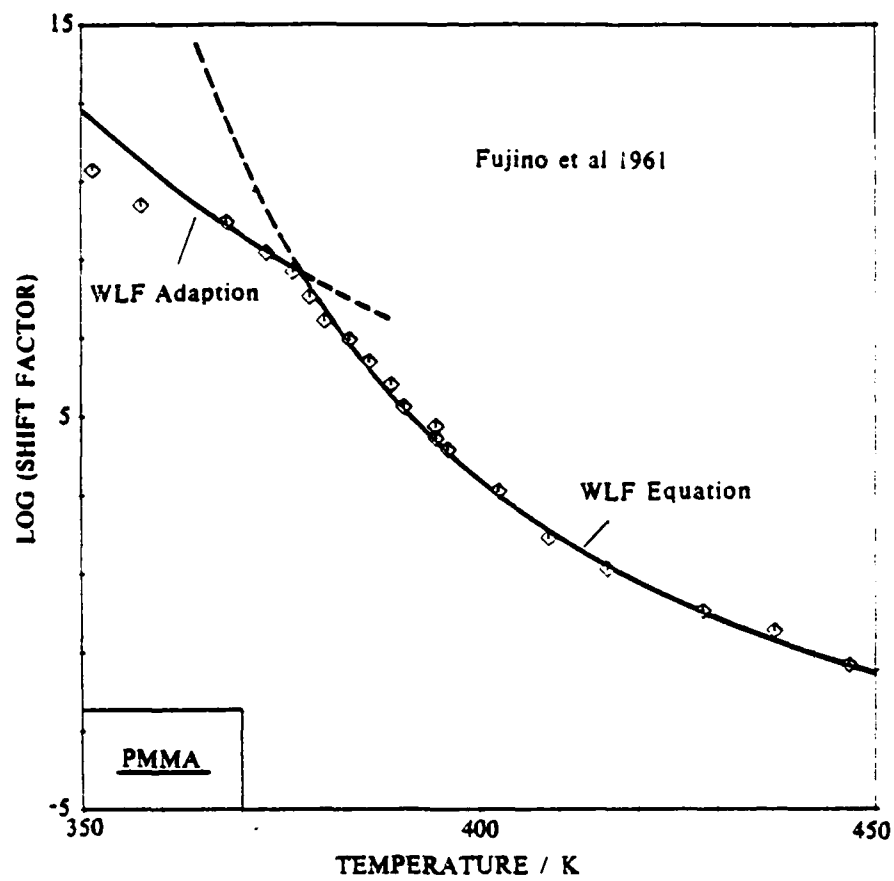


Fig. 15. The WLF shift factors calculated using the method of the text, compared with experiments (a) for PMMA, and (b) for PS.

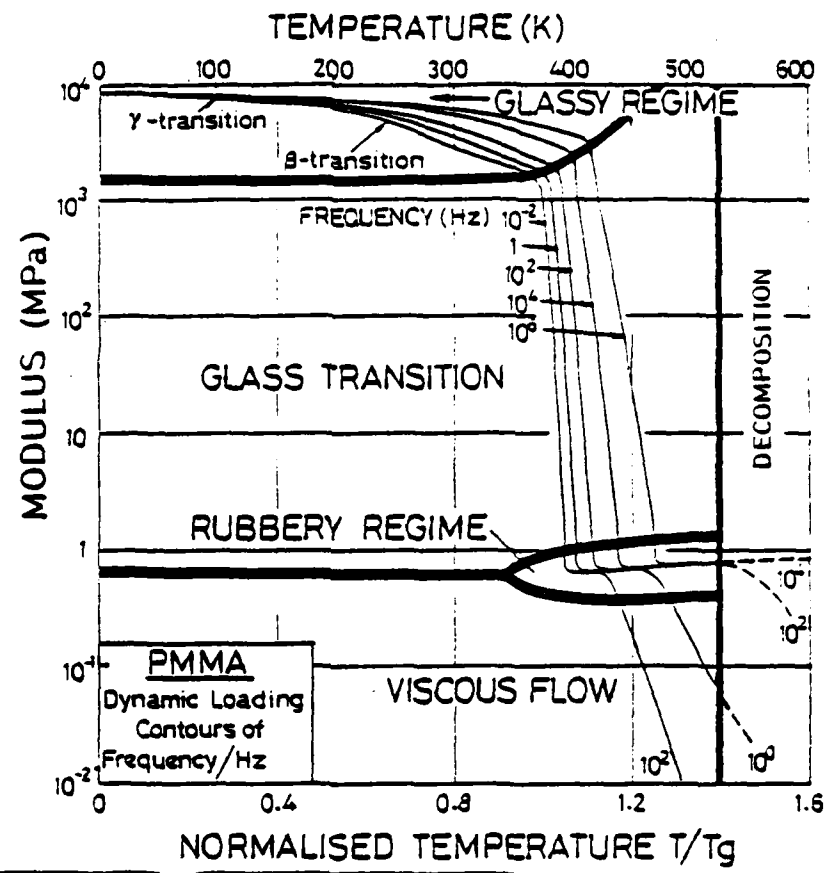


Fig. 16. A deformation diagram for PMMA under dynamic loading conditions, with E and T/T_g as axes.

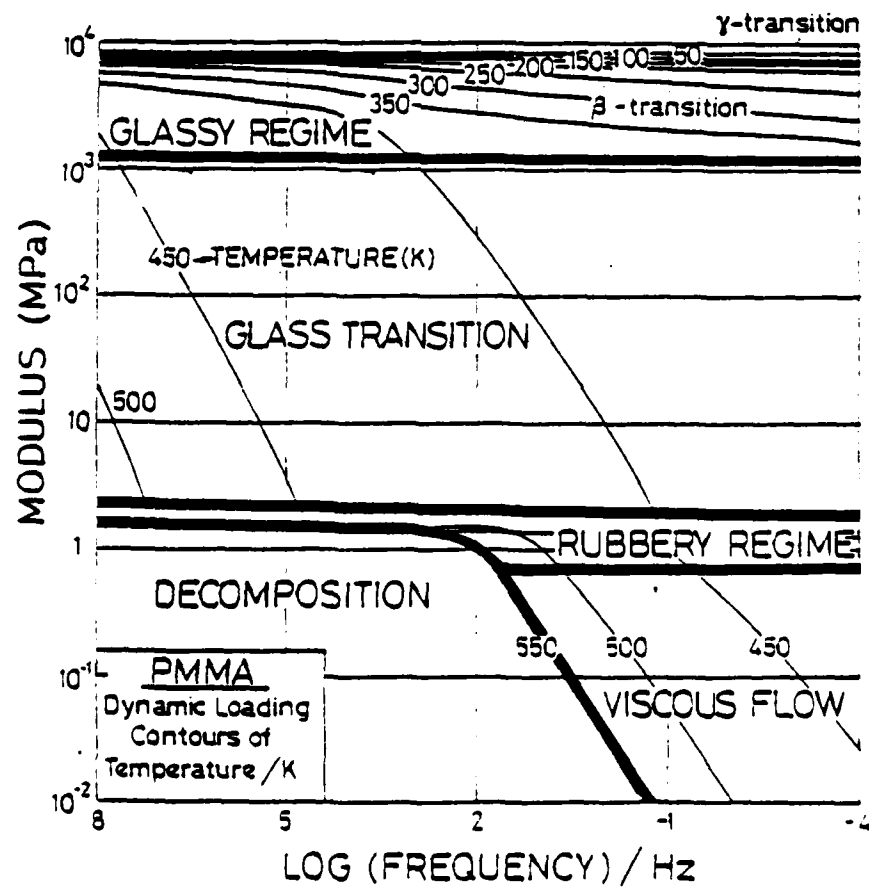


Fig. 17. A deformation diagram for PMMA under dynamic loading conditions, with E and frequency ν as axes. (The log ν scale is reversed to allow comparison with Figs. 20 and 22.)

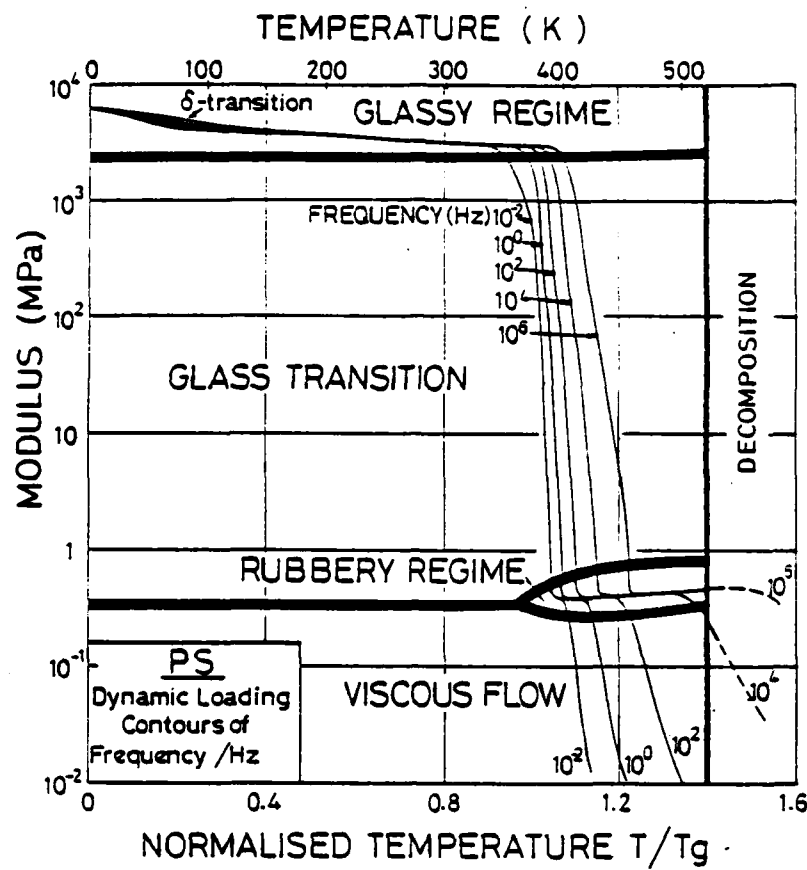


Fig. 18. A deformation diagram for PS under dynamic loading conditions, with E and T/T_g as axes.

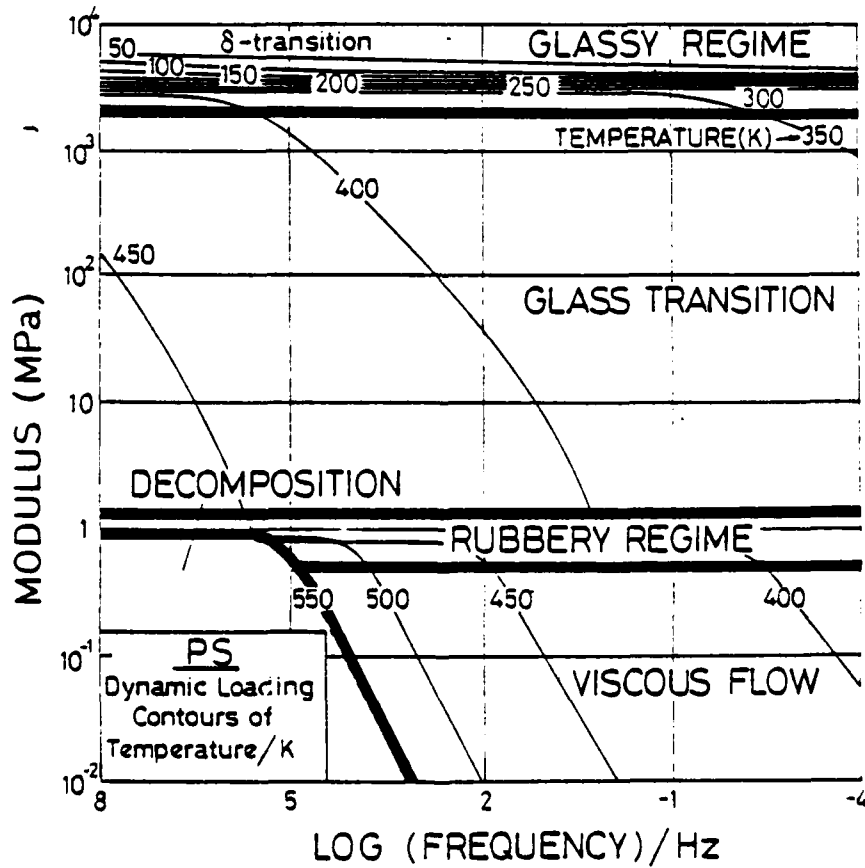


Fig. 19. A deformation diagram for PS under dynamic loading conditions with E and frequency v as axes. (The log v scale is reversed to allow comparison with Figs. 21 and 23.)

END

FILMED

1-86

DTIC